International Journal of Fatigue 180 (2024) 108102

Contents lists available at ScienceDirect

International Journal of Fatigue

journal homepage: www.elsevier.com/locate/ijfatigue

Influence of mean stress and building orientation on the fatigue properties of sub-unital thin-strut miniaturized Ti6Al4V specimens additively manufactured via Laser-Powder Bed Fusion

Simone Murchio [a,*], Anton Du Plessis [b,c], Valerio Luchin [d], Devid Maniglio [a,e], Matteo Benedetti [a,*]

[a] Department of Industrial Engineering – DII, University of Trento, Trento, Italy
[b] Research Group 3D Innovation, Stellenbosch University, Stellenbosch 7602, South Africa
[c] Object Research Systems, Montreal, Canada
[d] Lincotek Medical Trento, Pergine Valsugana, Italy
[e] BIOtech Research Center, University of Trento, Trento, Italy

ARTICLE INFO

Keywords:
Metal additive manufacturing
Laser-Powder Bed Fusion (L-PBF)
Fatigue strength
Sub-unital lattice structures
Mean stress effect

ABSTRACT

Fatigue is a complex, localized phenomenon affecting lattice structures at the level of struts and junctions. This study examines the fatigue properties of Laser-Powder Bed Fusion (L-PBF) Ti6Al4V miniaturized strut-like specimens, printed in four distinct building orientations (0°, 15°, 45°, 90°), and subjected to four stress ratios (R = 0.1, R = −1, R = −4, R = 10). Experimental data, summarized in Haigh diagrams, align well with predictions from the SWT and Walker methods. Notably, the dependency on mean stress diminishes as the building angle increases, attributed to progressively lower surface roughness which primarily drive failure at R = 0.1 and R = −1. In contrast, vertical specimens at R = −4 display a pronounced susceptibility to sub-surface defects affecting their fatigue strength, a finding corroborated by CT scan analyses. Additionally, the influence of buckling on fatigue performance is investigated and incorporated into the Haigh diagrams. These findings can contribute to a more informed design of L-PBF Ti6Al4V lattice structures against fatigue.

1. Introduction

Metal additive manufacturing (MAM), and particularly Laser-Powder Bed Fusion (L-PBF), has ushered in a new era of design and production for intricate components with specific functionalities [1]. These innovative manufacturing methods have enabled the use of architected cellular materials, opening up avenues for highly tailored applications due to their customizable mechanical properties [1–4]. For instance, the biomedical industry has started embracing lattice-based prosthetic devices manufactured through L-PBF, departing from traditional subtractive manufacturing techniques [4]. Despite the numerous advantages offered by MAM [1,5–8], such as expansive design possibilities, personalized customization, reduced stress-shielding, and limited implant subsidence, concerns regarding component structural integrity [7], the absence of AM-specific regulations [9,10], and the challenges of optimizing the manufacturing process parameters [11] have hindered widespread adoption of MAM components to critical highly stressed applications.

One crucial milestone in improving the practicality and safety of MAM components lies in enhancing the fatigue strength of lattice-based structures. Fatigue, a highly complex local phenomenon, is strongly influenced by manufacturing errors that may occur during the L-PBF process. Extensive efforts are currently underway to understand the fundamental fatigue behavior and fracture mechanisms of architected cellular materials. While much attention has been directed toward investigating the macro-scale fatigue properties of lattice components or individual cell units [12–16], fatigue predominantly manifests at the local scale [17,18]. The specific arrangement and design of interconnected struts in the lattice structure significantly influence stress distributions and crack propagation pathways. By examining local-scale fatigue phenomena within the lattice structure, such as the behavior of individual struts or junctions, critical areas prone to fatigue failure can be identified. These knowledges can enable the development of targeted strategies to enhance the overall fatigue resistance of lattice

* Corresponding authors.
E-mail addresses: simone.murchio@unitn.it (S. Murchio), matteo.benedetti@unitn.it (M. Benedetti).

https://doi.org/10.1016/j.ijfatigue.2023.108102
Received 26 October 2023; Received in revised form 6 December 2023; Accepted 9 December 2023
Available online 10 December 2023

components. Nonetheless, there has been limited focus on unravelling fatigue phenomena at a millimetric or sub-millimetric scale, particularly within the single struts or junctions of strut-based lattice cells [19–22]. The limited research on miniaturized specimens is primarily due to the absence of established AM standards and the ongoing uncertainty about whether miniaturized specimens can accurately represent and predict the properties of larger components [23]. While on one hand, the design of miniaturized specimens often fails to meet the requirements set forth by current normative, on the other hand, actual standards based on larger bulk specimens cannot adequately capture the spatial distribution of mechanical properties unique to AM components [23]. Moreover, the effect of build size and orientation on internal defects and surface roughness remains an area of ambiguity, with its influence on the mechanical and fatigue properties of AM components still a subject of active debate [23–26]. In this context, the investigation of building orientation has become increasingly crucial. A deepening on the relationship between build orientation and the resulting mechanical properties is therefore of paramount importance towards the definition of new standards suitable for AM components.

Whitin this context, it is well-known that L-PBF components, in their as-built condition, are strongly influenced by factors such as high surface texture, parasitic mass formation, dross, and sub-surface defects of their sub-unit elements [24,27–29]. These factors contribute to the relatively poor fatigue life of additively manufactured Ti6Al4V components compared to the wrought material. Additionally, the high surface-to-volume ratio associated with small specimen size and the specimen building orientation are fundamental factors affecting defect sensitivity and distribution at the local scale [30]. The role of the building orientation is strongly related to the different heat transfer characteristics occurring during the solidification process of the powder. Factors such as the spatial location of the solidified powder, the ratio of solid to unsolidified powder, and the apparent density of the powder influence heat transfer. Since unsolidified powder has lower conductivity than solidified powder, heat is primarily dissipated through the solidified metal. As a result, when a strut is positioned parallel to the building plane, is only supported by less conductive powder, hence, a substantial melt pool forms [31]. Furthermore, due to gravitational and capillary effects, the molten metal tends to flow into the powder, leading to an enlarged strut with surface irregularities, particularly on the lower side [32]. Conversely, vertical struts exhibit a smaller and more homogeneous melt pool, resulting in reduced geometric imperfections and higher geometric accuracy [19,33]. Inclined struts display a distinctive “staircase” profile due to the offset between adjacent layers welded together as a result of strut inclination, leading again to sever mismatches with respect to the nominal design model [34]. The fluctuations and irregularities introduced by the building orientation severely impact the overall mechanical and fatigue properties of a lattice component, detrimentally affecting its structural integrity. For instance, *Wu et al.* [35] demonstrated a pronounced anisotropic fatigue resistance in L-PBF AlSi10Mg components, depending on whether they were built parallel or perpendicular to the building direction. The authors attributed this significant variation in fatigue strength to the increased presence of Lack-of-Fusion (LoF) defects of larger projected area on the axial perpendicular plane in components printed parallel to the build direction. Further expanding on this topic, *Carrion et al.* [36] explored the influence of the building orientation on the fatigue behaviour of L-PBF Ti6Al4V hollow pipe samples, subjected both to axial and torsional loadings. Their findings revealed a synergistic impact of building orientation, surface defectiveness, and multiaxial loading on the fatigue strength of these specimens. Notably, they underscored the more severe detrimental effect of surface micro-notches on 45° titled specimens under torsional loading with respect to vertically printed component. The enhanced vulnerability of 45° specimens was attributed to the alignment of surface micro-notches with the maximum principal stress plane, oriented at 45°/135°.

Hence, in the context of evaluating the structural integrity and enhancing the fatigue resistance of MAM components, it is also crucial to consider a wide range of complex loading conditions under which a component might be. This is especially true for lattice-based prosthetic devices, such as spinal implant cages or hip stems. Although these devices primarily experience high compressive loads, at the unit cell scale, various fatigue loading scenarios can occur, subjecting individual struts to different fatigue regimes. Accounting for these diverse stress conditions becomes paramount in assessing the overall performance and durability of such prosthetic devices.

Few studies investigated the role of mean stress effects on the axial fatigue strength of Ti6Al4V architected cellular materials, primarily focusing on the role of the unit cell, particularly in a compression-compression fatigue regime [37,38]. *Lietaert et al.* [14], extended the analysis to tension-tension regimes, investigating the role of mean stress effects on the fatigue properties of diamond unit cells under different loading conditions.

Solely focusing on the role of Ti6Al4V L-PBF coupon specimens under various fatigue regimes, *Benedetti et al.* [39] conducted fatigue tests on samples treated with different post-processing methods and under three different stress ratios. The authors reported a good correlation between the experimental data and the Smith-Watson-Topper (SWT) mean stress model. *Derrick & Fatemi* [40] extensively reviewed various studies on the fatigue behavior of additive manufactured (AM) metals, specifically focusing on as-built L-PBF Ti-6Al-4V samples tested under different stress ratios. The authors concluded that the SWT method is a dependable predictive tool in tensile conditions, while Walker’s equation yields better agreement with experimental results when the mean stress is compressive. Recently, *Cutolo et al.* [41] investigated the influence of positive mean stress range on as-built and post-processed L-PBF Ti6Al4V coupons, confirming that the exponential Walker’s equation can provide a reliable prediction of the experimental results for as-built components. However, to the authors’ best knowledge, no study has focused on the role of different load ratios according to the different building directions of miniaturized specimens resembling the struts of strut-based lattices.

In this study, we aim to investigate the fatigue behavior of miniaturized strut-like specimens under different loading stress ratios, R, and building orientations. The present paper initially focuses on the design and manufacturing of the thin struts according to four building orientations: 90° (vertical), 45°, 15°, and 0° (horizontal) with respect to the build plate. Then it moves to the determination of the true cross-sectional area of each investigated strut employing a cost-effective stereo-optical metrological analysis. The latter allows us to explore the relationship between mechanical behavior, monotonic and fatigue properties, and printing outcomes, including associated defects. The monotonic properties are investigated, with a peculiar focus on the buckling instability and its analytical prediction. Consequently, a thorough fatigue testing campaign is performed, with specimens subjected to various fatigue regimes, specifically under tension–tension ($R = 0.1$), tension–compression ($R = -1$), 25 % tension-75 % compression ($R = -4$), and compression-compression ($R = 10$). Furthermore, we focus on the distinct fatigue failure mechanisms associated with different fatigue regimes at different building orientations. The role of surface and sub-surface defects is therefore assessed by using scanning electron microscopy (SEM) investigation of the fracture surfaces and by computed tomography (CT) scans. The mean stress effect is then accounted by means of the Haigh diagram, evaluating several mean stress predictive models, their correlation with experimental data, taking also into account buckling instabilities. These diagrams provide valuable insight for the fatigue life at varying alternating loads and building orientations of L-PBF Ti6Al4V miniaturized components.

2. Materials and methods

2.1. Specimen design and manufacturing

Miniaturized dog-bone specimens, resembling struts of lattice-based architected cellular materials, were designed with a nominal thickness of 0.67 mm and a gauge length of 2.4 mm. The total length of the specimen was set to 15 mm, including two gripping sections of 5 mm length each and a transition zone at the grip/gauge length interface. The latter was designed by adopting the stream fillet approach proposed in [42] aimed at mitigating the stress concentration factors which might arise at the grip/gauge length interface. It is important to acknowledge that, although fatigue failure can occur at junctions in lattices, this study focuses exclusively on the fatigue behavior of thin struts within lattice structures. This approach intentionally separates the study of struts from the influences of junctions. Therefore, the stream fillet method was carefully chosen to minimize potential biases caused by systematic failures at the interface of gripping and gauge lengths. For a detailed exploration of the impact of junctions on lattice fatigue, we refer readers to our previous research [20].

The miniaturized thin-strut specimens were additively manufactured via L-PBF, employing a biomedical graded Ti-6Al-4V Grade 5 spherical powder ($O_2 < 0.2$ %) of size in the 15–45 µm range. The specimens were printed at Lincotek Medical's facilities (Trento, Italy), by means of an EOS M290 printer equipped with a 400 W laser, and a layer thickness of 60 µm. This and the other L-PBF process parameters reported in this study were determined by our industrial partner to strike a balance between productivity and manufacturing accuracy. It is important to acknowledge that prioritizing manufacturing accuracy, such as using a lower layer thickness value, could potentially improve the quality of the printed components. However, this would come at the expense of lower process productivity and, as a result, increased manufacturing cost. The selection of these process parameters was made to ensure that the results obtained from this study would be representative of real industrial applications, where achieving a balance between accuracy and productivity is crucial.

Once fabricated, the specimens underwent a heat treatment at temperatures above 800 °C to remove residual stresses and transform the α-martensitic as-built microstructure to a more stable α + β lamellar structure. Four batches of dog-bone specimens were printed according to four different building orientations, namely at 90°,45°, 15°, and 0° with respect to the build plate, as reported in Fig. 1. The specimens are in their as-built condition since no post-processing surface treatment was applied. Additionally, a minimum number of supporting structures (as noticeable in light grey, in Fig. 1b) was intentionally placed along the small section of the grips, aimed at leaving the gauge length fully unsupported, thus better mimicking the printing conditions of intricate strut-based lattice components. Specimens were detached from the base supporting structure via Electron Discharge Machining (EDM). Remaining supporting structures were removed by means of wire cutters

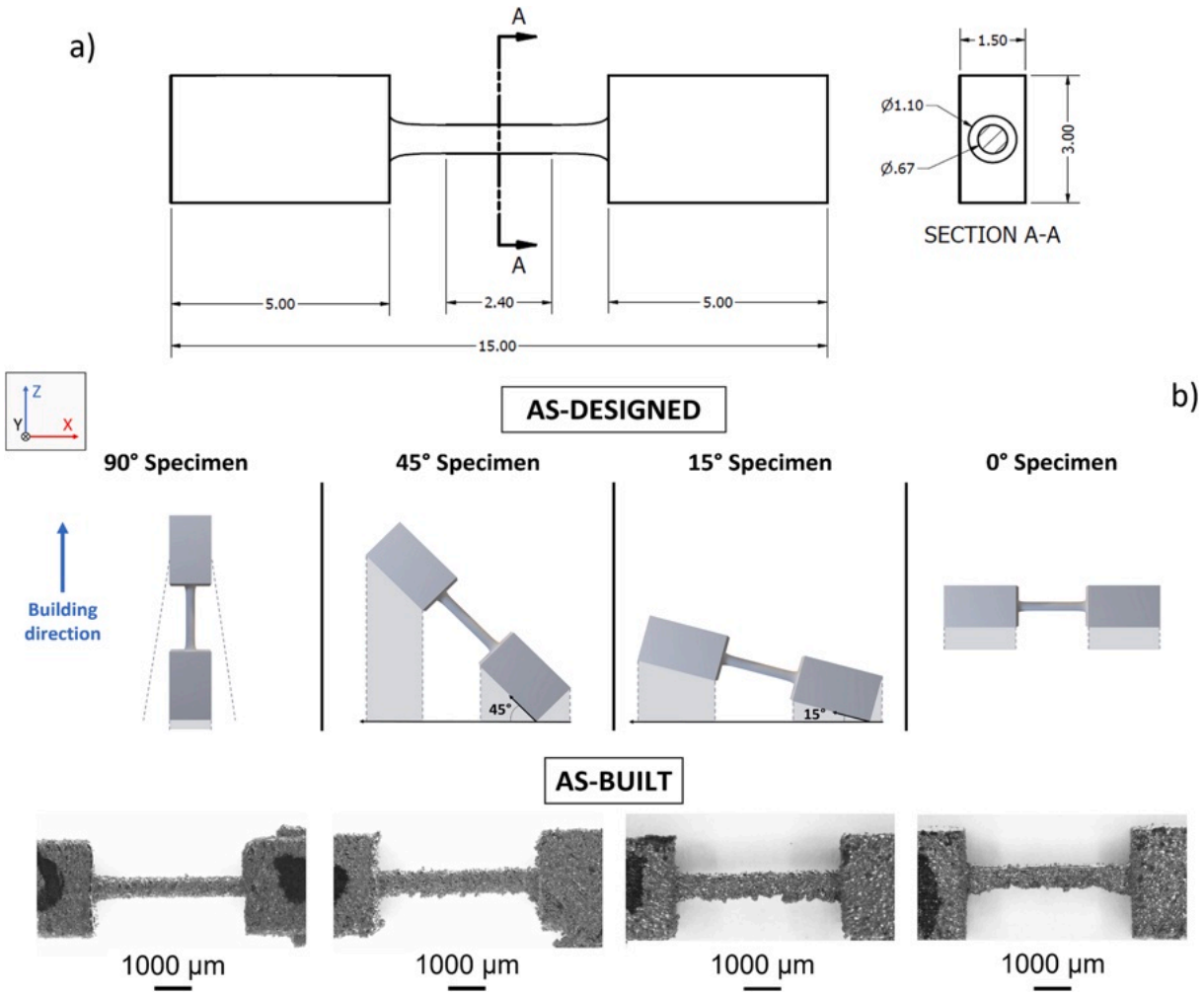

Fig. 1. a) Technical drawing of the thin-strut dog-bone like specimens. Measures are set in mm. b) As designed specimens according to the four different building orientations, namely at 90°, 45°,15° and 0° with respect to the build plate. Support structures are highlighted in light grey. Four images of the as-built specimens captured by a stereo-optical microscope can show the different manufacturing process according to the building orientation.

or nippers, without compromising the specimen integrity. Furthermore, specimens with gauge length interruption or severe and unexpected geometrical deviations from the nominal design (i.e., severe cross-sectional thinning, evident printing errors, or severe waviness) were excluded from the inspected batches, to avoid biased analyses.

2.2. Experimental analysis

2.2.1. Morphological and microstructural characterization

The morphological characterization of the specimens was carried out employing a fast and cost-effective stereo-optical approach, as described in [19,43]. Briefly, a Nikon SMZ25 stereo microscope was adopted to collect two pictures for each inspected specimen and an in-house MATLAB routine was employed for the image analysis. The latter provided information concerning some of the main geometrical features of thin-strut specimens, such as strut thickness, cross-sectional area, eccentricity, and deviations from the as-designed nominal geometry. The sampling step between two measured thickness data was set to 3.5 μm for each tested batch.

All the geometrical data were collected before the mechanical testing and an assumption of elliptical cross-section was adopted for every differently oriented specimen [19]. Three different cross-sections were considered, namely the nominal (as-designed), the minimum cross-section, measurable along the gauge length of each specimen, and the average cross-section, obtained by averaging all the sampled areas calculated within the gauge length of the inspected thin-strut specimen. The author from now on will refer to these cross-sections, respectively as, "nominal", "minimum" and "average" cross-sections.

The surface roughness characterization of thin struts was conducted using an Olympus DSX100 High-Resolution Opto-digital microscope, equipped with a 20x objective lens. The DSX10-BSW software was employed for surface roughness analysis. Each specimen underwent five distinct measurements, both for their upper and lower skins. Measurements were collected on three specimens for each build orientation. It is important to note that the miniaturized dimensions of the strut specimens made it impractical to fully adhere to the guidelines of the ISO standard (ISO 4288:1996). The challenge of applying existing standards to lattice components fabricated through AM is well-documented in the literature, and there is ongoing debate about the appropriate parameters to be used in such cases. Following the approach detailed in the work of *Nagalingam et al.* [44], which provides a comprehensive discussion on this subject, we maintained compliance with the ISO standard's recommendation for the cut-off wavelength, λc, setting it at 2.5 mm. This decision necessitated a compromise in terms of the total evaluation length. However, since the surface roughness measurements were used for comparative purposes and executed consistently across all specimens, the impact of the reduced test length is deemed to be uniform and, as such, can be reasonably disregarded. This approach is also in line with findings presented in [45,46].

Metallographic analyses were conducted to characterize the specimens. Two samples for each building orientation, namely at 90° and 0°, were analyzed either along the parallel or the perpendicular sections with respect to the axial loading axis. The sample preparation initially involved a cold mounting process, through a PRESI epoxy resin and a hardener in the ratio of 10:1. The hardening time was set to 8 h before the grinding and polishing stages. Five grinding steps of the investigated sections with SiC abrasive papers of 240, 500, 800, 1200, and 4000 grit sizes were performed prior to polishing. The latter was performed with a 3 μm and 1 μm diamond paste, respectively. Finally, the specimens underwent active oxide polishing (OP-S), exploiting a colloidal silica suspension. Additionally, to obtain mirror-like surfaces, an etching process with Weck's reagent was done. Metallographic images were then collected using a Zeiss Axiophot (Zeiss, Germany) light optical microscope.

2.2.2. Monotonic properties: Tensile and compressive tests

Tensile and compressive tests were carried out using an Instron 4502 testing machine equipped with a 1 kN load cell. The crosshead speed was set to 0.1 mm/min and the acquiring sample rate to 2 pts/sec. Three samples for each batch were tested. Due to the miniaturized dimension of the specimens, it was not feasible to apply an extensometer to the gauge length. The stress–strain curves were derived based on the displacement of the crossbar, incorporating adjustments to account for machine compliance. Young's modulus was obtained from the linear section of the elastic region of the stress–strain curve. The yield strength, σ_y, was obtained with the 0.2 % offset yield method. From the stress–-strain curves, additional data, such as the yield strain, the ultimate tensile/compressive strength (UTS and UCS), and the associated strains were also evaluated.

Thin struts can often fail due to buckling instability if subjected to static or dynamic compressive regimes. This generally occurs at lower force values than for tensile failure [47]. Buckling can be usually determined through the critical buckling load, obtained by experimental analyses or by predicting analytic or numerical approaches. As stated in [47], due to the manufacturing defects intrinsically generated by additive manufacturing processes, the classical Euler's formula cannot be anymore considered reliable, particularly for short columns. In this work, an analytic prediction of the buckling phenomena was obtained by employing Johnson's approach. This approach is more conservative, with respect to the Euler approach, in predicting the critical column strength of short or intermediate columns also subjected to inelastic buckling behavior. The critical buckling strength can be determined according to *Eq. (1)*:

$$\sigma_{cr} = \sigma_y - \frac{1}{E}\left(\frac{\sigma_y}{2\pi}\right)^2 \left(\frac{l}{k}\right)^2 \tag{1}$$

where σ_y is the compressive yield strength, E is the elastic modulus, and $\frac{l}{k}$ is the slenderness ratio of the strut (with k as the radius of gyration). The slenderness ratio can be also expressed as a function of the effective length of the column L_e, the column cross-section A, and the area moment of inertia of the column cross-section I, as reported in *Eq. (2)*:

$$\frac{l}{k} = L_e\sqrt{\frac{A}{I}} \tag{2}$$

The effective length of the column L_e is then calculated as the product of the column length L for a theoretical or recommended coefficient c. In the case of thin struts under compression testing, rotation and translation of the column ends are hindered. A rigidly fixed constraint is thus considered and to which a c = 0.5 and c = 0.65 are respectively associated.

2.2.3. Fatigue tests

Fatigue tests were carried out using a Bose Electroforce 3200 testing machine, equipped with load cell full scale of ±200 N and a load cell sensitivity of ±0.05 N. The testing machine is equipped with a mechanical gripping system in stainless steel and with a clamp design with knurled screws for locking. Tests were performed at a nominal frequency of 200 Hz, in a sinusoidal waveform, and a load-controlled regime, in air and at room temperature. Four different stress ratios were investigated for the four building orientations. Namely, fatigue tests encompass a R = −1 (fully reversible fatigue cycle of tension–compression), a R = −4 (tension–compression cycle with a more pronounced compressive phase), a R = 0.1 (tension–tension fatigue cycle) and a R = 10 (compression-compression cycle) fatigue regime. For the latter stress ratio, R = 10, the nominal frequency was reduced to 50 Hz, due to machine limitation on the allowable frequency when the maximum stresses approach the load cell full scale. Nonetheless, within this range, the effect of the frequency is expected to be negligible on the fatigue strength of the tested specimens. It is also worth noting that any specific international standard could be applied in the design phase of these

specimens, due to their miniaturized size. For all four stress ratios, fatigue tests were conducted until specimens either failed or reached a predetermined fatigue life set at 10^7 cycles. This value was identified by a horizontal arrow on the S-N fatigue plots. Run-out specimens were reused at an applied load 1.5 times higher than the original, so to extend and increase the experimental data points for the non-linear fitting of the S-N fatigue curves. A minimum of 12 samples per condition were tested and 2–3 specimens per load step were considered. As explained in [19], Wöhler's curves were fitted according to *Eq. (3)*:

$$\sigma_a = C_1 + \frac{C_2}{N_f^{c_3}} \tag{3}$$

where C_1, C_2, and C_3 are the constants to be fitted, N_f is the number of cycles upon failure or runout and σ_a is the stress amplitude. The scatter bands at 10 % and 90 % failure probability are also reported and have been calculated considering a uniform regression variance throughout the whole tested range. These bands can be consequently calculated as follow in *Eq. (4)*:

$$S^2 = \frac{\sum_{i=1}^{n}\left(\sigma_{a,i} - \widehat{\sigma}_{a,i}\right)^2}{n-p} \tag{4}$$

where $\sigma_{a,i}$ is the i.th fatigue amplitude, $\widehat{\sigma}_{a,i}$ its estimator. The parameters, n and p, are the numbers of collected data and the number of regression parameters involved in *Eq. (3)*, thus set to 3.

The fatigue data were then employed to build the Haigh diagram for an evaluation of the mean stress effect on the thin-strut fatigue properties according to different stress ratios. Four different correlation methods between the means stress and the amplitude stress have been investigated and discussed. Particularly, the Goodman-modified criterion, reported in *Eq. (4.1)*; the Smith-Watson-Topper (SWT) method, in *Eq. (4.2)*; the FKM method, shown in *Eq. (4.3)*, and the Walker method in *Eq. (4.4)*:

$$\frac{\sigma_a}{\sigma_{a,eq}} + \frac{\sigma_m}{\sigma_{uts}} = 1 \tag{4.1}$$

$$\sigma_{a,eq} = \sqrt{\sigma_{max}\sigma_a} \tag{4.2}$$

$$\sigma_{a,eq} = \begin{cases} \sigma_a(1-M_\sigma), & \text{Region I} \quad R \geq -\infty \\ \sigma_a + M_\sigma\sigma_m, & \text{Region II} \quad -\infty < R \leq 0 \\ (1+M_\sigma)\dfrac{\sigma_a + \left(\frac{M_\sigma}{3}\right)\sigma_m}{1+\left(\frac{M_\sigma}{3}\right)}, & \text{Region III} \quad 0 < R \leq 0.5 \\ \sigma_a\dfrac{3(1+M_\sigma)^2}{3+M_\sigma}, & \text{Region IV} \quad R > 0.5 \end{cases} \tag{4.3}$$

$$\sigma_{a,eq} = \sigma_{max}^{1-\alpha}\sigma_a^{\alpha} \tag{4.4}$$

where $\sigma_{a,eq}$ is the equivalent amplitude stress, σ_a is the amplitude stress, σ_m is the mean stress, σ_{uts} the ultimate tensile strength (calculated in the work of *Murchio et al.* [19]) and σ_{max} the maximum stress under the fatigue regime. For the FKM criteria, the M_σ mean sensitivity parameter must be calculated. The latter is calculated as reported in *Eq. (5)*:

$$M_\sigma = a_M 10^{-3}\sigma_{UTS} + b_M \tag{5}$$

where a_M and b_M are material-related parameters, respectively set at 0.45 and −0.04 for Titanium alloys [48]. Coefficient α in *Eq. (4.4)* can be calculated by fitting procedures of the experimental data points.

2.2.4. Surface fracture analysis

A Zeiss supra 40 (Zeiss, Germany) Field-Emission Scanning Electron Microscopy (FE-SEM) was used to inspect the fracture surfaces of the tensile-failed and fatigue-failed thin-strut specimens. The images were acquired at a 5.00 kV acceleration in a secondary electron mode. Three samples per building orientation and for each stress ratio were inspected, considering both sides of the fracture surface of each specimen. To remove potential debris or dust on the fracture surfaces, the whole inspected specimens underwent an ultrasonication cleaning procedure in ethanol for 15 min before the analysis.

2.2.5. X-ray computed tomography

X-ray computed tomography was performed using a General Electric Vtomex L240 microCT system at Stellenbosch University. Scans were performed with settings to optimize image quality and a voxel size of 5 μm was obtained. Images were analyzed in Dragonfly version 2022.2, with segmentation by Otsu thresholding. An example of a sample built at zero degrees is shown below in Fig. 2, showing from left to right CT images of the sample porosity, expressed in the form of equivalent diameter (in μm) and the surface view.

CT defect data were analyzed according to their morphological (sphericity) and dimensional parameters (minimum distance from the outermost surface and size). Defect size has to be considered as the Murakami's parameter [49], $\sqrt{area}$, which is the square root of the defect projected area on the plane perpendicular to the axial loading direction. The role of defects for the four building orientations was investigated by means of the statistics of extremes [50] , by employing the Peak-Over-Threshold (POT) approach [51,52]. Briefly, this method is based on the selection of a threshold u and the consequent sampling of the exceedances above this threshold value, so that $x : x \geq u$. The defect data population -exceedances- report properties comparable to the ones od extreme values distributions, and specifically of a Generalized Pareto Distribution (GPD), as reported in *Eq. (6)*:

$$W_{\gamma,u,\sigma}(x) = 1 - \left(1 + \gamma\frac{x-u}{\sigma}\right)^{-\frac{1}{\gamma}} \tag{6}$$

where γ and σ are respectively the shape and scale parameters, which can be calculated by employing the Maximum Likelihood (ML) method. In the case the shape parameter γ is approaching zero, the cumulative distribution function can be simplified to an exponential distribution, as reported in *Eq. (7)*:

$$W_{\gamma,u,\sigma}(x) = 1 - e^{-\frac{x-u}{\sigma}} \tag{7}$$

By applying the fundamental concepts of the extreme value statistics, the modal value of the maximum defect in a given volume V_c can be defined as reported in *Eq. (8)*:

$$x_{max,V_c} = W_{\gamma,u,\sigma}^{-1}\left(1 - \frac{1}{T}\right) \tag{8}$$

where T is the return period of the maximum defect. If the scale parameter $\gamma \to 0$, the calculation of the maximum defect size can be achieved as shown in *Eq. (9)*:

$$x_{max,V_c} = u + \sigma \bullet \ln(T) \tag{9}$$

The defect data analysis was performed either considering the entire scan volume V_{POT} as well as a toroidal volume V_s, including the entire population of defects at a distance from the surface ≤ 100 μm, approximately approaching the contour thickness adopted in the specimen printing strategy. The POT threshold, u, was selected by means of the mean excess plots, as reported in [51,53], and set at 15 μm. The threshold choice also allowed to cut off all the defects close to the CT scan resolution limit.

3. Results and discussion

3.1. Morphological characterization

Fig. 3 presents a comparative analysis of geometrical parameters obtained from stereo-optical-based metrological analysis. Bar graphs in

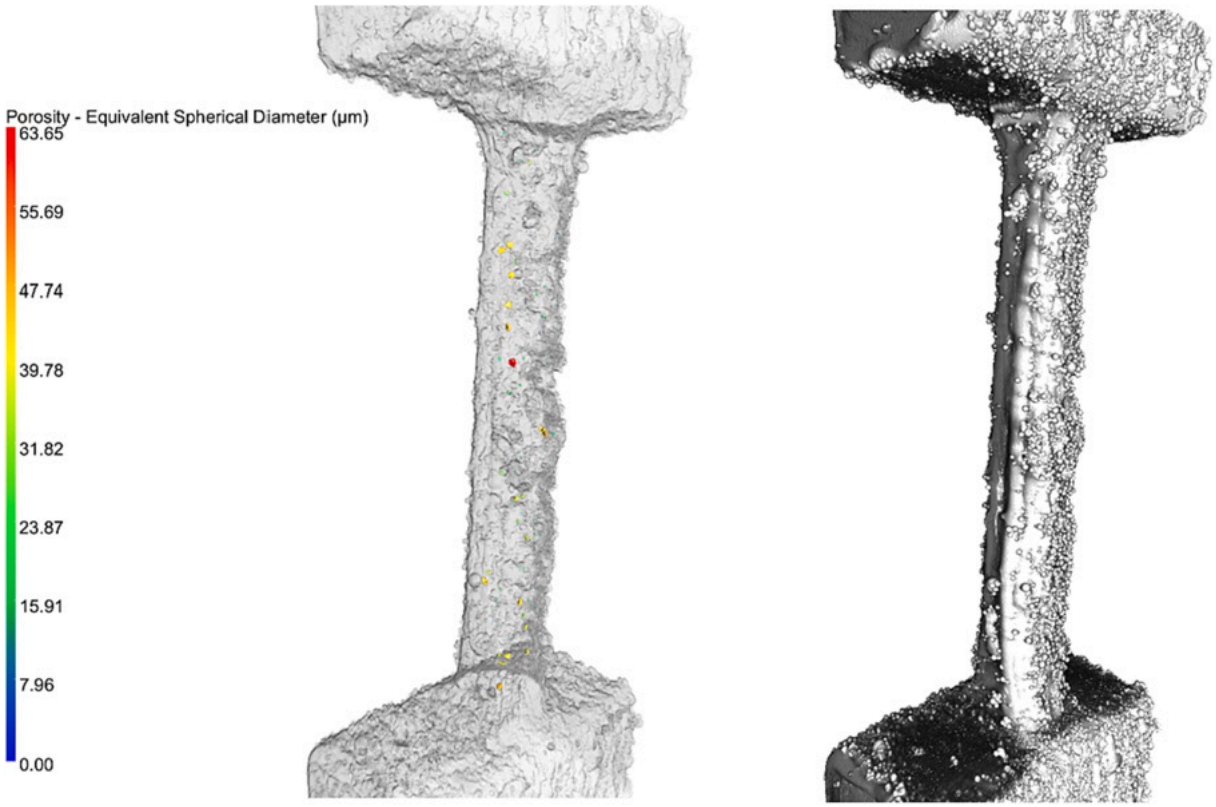

Fig. 2. Example CT scan images of a thin strut printed at 0°. The left image shows the sample internal porosity, with the associated colored scale bar. Sample porosity is expressed as the equivalent spherical diameter in μm. On the right, the rendering of the external surface is shown.

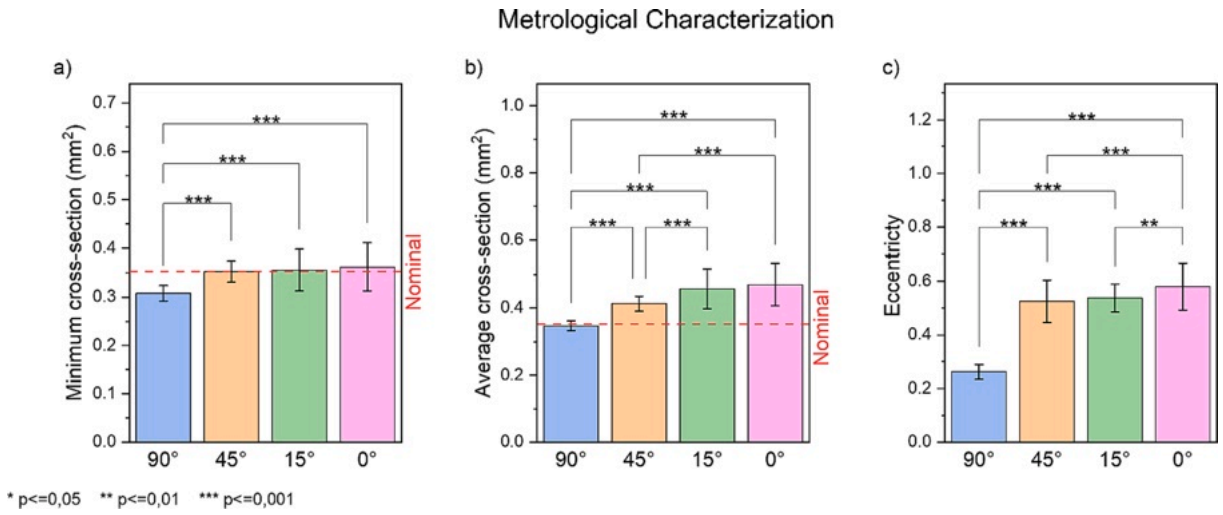

Fig. 3. Comparative bar plots of the minimum (a), average cross-sections (b), and eccentricity (c) of the four inspected orientations, namely at 90° (blue), 45° (orange), 15° (green), and 0° (purple). One-way ANOVA with Tukey's test was performed to make the statistical comparison ($p <= 0.05$), as reported in the graphs' label. Red dashed line referring to the nominal cross-section area is also reported in Figure (a) and (b).

Fig. 3a, 3b, and 3c depict the minimum, average cross-section, and eccentricity, respectively, for four different building orientations. A One-way ANOVA followed by Tukey's test was conducted to investigate differences induced by printing orientation. The vertically oriented specimens consistently exhibited statistically significant differences compared to less inclined thin struts. The 90° specimens showed the lowest values for cross-sectional evaluation (minimum cross-section: 0.308 ± 0.016 mm2; average cross-section: 0.347 ± 0.015 mm2) and eccentricity (0.26 ± 0.03), indicating a more circular cross-section. However, these values were slightly lower than the nominal design, as evidenced by the negative deviation (−13 ± 4 % and −2 ± 4 % for minimum and average area, respectively) in Table 1. This deviation is attributed to a more uniform solidification process with solid supports throughout the printing, ensuring higher uniformity in the melt pool and hindering the attachment of unmolten powder particles. Inclined and horizontal specimens exhibited the "stair-case effect" and were influenced by capillary and gravitational effects, leading to a more heterogeneous and larger melt pool. Consequently, the geometrical outcomes of inclined and horizontal specimens deviated significantly from the nominal design, with a loss of circularity and an increase in eccentric

Table 1
Minimum and average cross-section (mm^2), deviation from nominal design (in %), average and minimum thickness (μm) and eccentricity for the four inspected orientations. Data are reported as mean values, calculated over the whole batch of specimens, along with their standard deviation.

	90°		45°		15°		0°	
	Minimum	**Average**	**Minimum**	**Average**	**Minimum**	**Average**	**Minimum**	**Average**
Cross section (mm^2)	0.308 ± 0.016	0.347 ± 0.015	0.346 ± 0.051	0.405 ± 0.059	0.349 ± 0.062	0.448 ± 0.082	0.355 ± 0.067	0.461 ± 0.086
Dev. from CAD (%)	−13 ± 4	−2 ± 4	−2 ± 15	−15 ± 17	−1 ± 18	27 ± 23	1 ± 19	31 ± 24
Thickness (μm)	606 ± 18	664 ± 14	595 ± 85	714 ± 102	608 ± 92	750 ± 116	601 ± 92	776 ± 119
Dev. from CAD (%)	−10 ± 3	−1 ± 2	−11 ± 13	7 ± 15	−9 ± 14	12 ± 17	−10 ± 14	14 ± 18
Eccentricity	0.26 ± 0.03		0.52 ± 0.10		0.53 ± 0.09		0.57 ± 0.11	

cross-sections. Fig. 3c and Table 1 demonstrate an increase in eccentricity from 0.26 ± 0.03 for vertical struts to 0.57 ± 0.11 for horizontal specimens. These process-induced deviations not only affect the geometrical outcome but also impact the mechanical behavior of the specimens [21,54], as discussed in *Section 3.3.*. The fluctuations in the standard deviation of the specimens indicate manufacturing-induced scattering and emphasize the need for better control of process parameters. The average morphological properties are used to calculate global mechanical properties, while the minimum cross-section assesses fatigue behavior, as further discussed in the following sections.

In their as-built conditions, L-PBF specimens frequently display pronounced surface texture, as noticeable from Fig. 1b. This characteristic is often identified as a key contributor to fatigue failure in architected cellular materials [55]. Fig. 4 presents bar plots depicting the mean surface roughness for each of the four distinct batches. The analysis separately addresses the roughness on both the upper and lower surfaces of struts, for inclined or horizontal. Vertical specimens do not report any skin distinction, due to the complete material deposition over a dense layer. Three representative surface roughness estimators are considered: *Ra* (shown in Fig. 4a), *Rz* (Fig. 4b), and *Rv* (Fig. 4c). To elucidate potential statistical differences among the batches, a One-Way ANOVA, complemented by a post-hoc Tukey's test, was performed.

The 90° specimens exhibit the lowest surface roughness values across all three estimators, with specific values for *Ra*, *Rv*, and *Rz* of 13 μm, 35.7 μm and 81.4 μm. A clear influence of build orientation is observed, particularly when examining specimens oriented at lower angles. A notable increasing trend in surface roughness is evident, especially in specimens oriented at 15° and 0°, which exhibit the highest roughness values on their lower skin. These findings align with our prior research on similarly printed struts using identical print parameters and comparable geometries [19]. For a detailed numerical comparison of these average values, readers are directed to *Table S1* in the *Supplementary Material*.

3.2. Microstructural analysis

The microstructures of L-PBF Ti6Al4V thin struts printed at 90° and 0° orientations are depicted in Fig. 5. These figures show the microstructural images of the specimens as inspected on two different slices: one perpendicular to the axial load direction (X′Y′), and one parallel to it (X′Z′ or Y′Z′).

The images reveal a coarse α lamellar phase (light) embedded in a β matrix (dark) in both specimens. The heat treatment was effective in transforming the brittle, acicular α' phase into a more ductile and coarser α + β lamellar structure. The 90° thin strut specimen (Fig. 5a) exhibits randomly distributed prior columnar grains in the X′Y′ cross-sectional area, while the Y′Z′ section shows grains partially aligned with the build direction. The 0° thin strut specimen (Fig. 5b) exhibits grains slightly aligned with the build direction in both the X′Y′ and X′Z′ sections. These microstructures are consistent with those reported in the literature, specifically in the work of *Agius et al.* [56], for L-PBF Ti6Al4V thin struts printed at different orientations after heat treatment.

3.3. Fatigue behavior

In this section, the fatigue properties of Ti-6Al-4V thin struts are reported. A discussion on the influence of the building orientation effect and the different stress ratios is carried out in *Section 3.3.1* and *Section 3.3.2*, respectively. Additionally, the influence of the surface texture and inner defectiveness on the fatigue failure.

mechanisms is discussed in *Section 3.3.3*, where an SEM investigation of the fracture surfaces of the specimens is reported. CT scans of the specimens along with a statistical analysis of the population defects is also reported to support the SEM investigation.

3.3.1. Influence of building orientation

The S-N curves in a semi-logarithmic scale for the four different specimen orientations are reported in Fig. 6a-d, namely for R = 0.1, R = −1, R = −4, and R = 10. For sake of clarity, it is worth noting that the stress amplitude has been calculated considering the minimum cross-

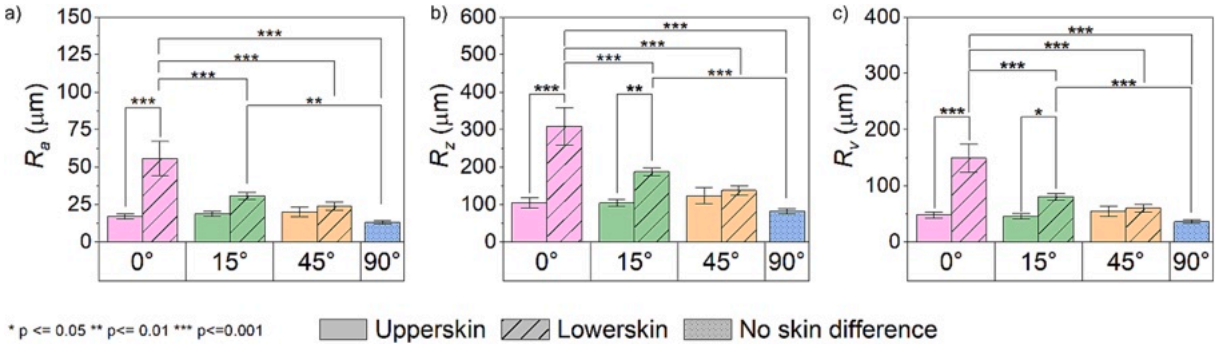

Fig. 4. Comparative bar plots of three surface roughness estimators: Ra (a), Rz (b), and Rv (c) of the four inspected orientations, namely at 90° (blue), 45° (orange), 15° (green), and 0° (purple). Measurements were divided for upperskin (labeled as bars with no pattern) and lowerskin (labeled as bars with diagonal sparse pattern) for inclined and horizontal specimens. No distinction has been done between skins for vertical specimens (labeled as bars with dotted pattern). One-way ANOVA with Tukey's test was performed to make the statistical comparison (p<= 0.05), as reported in the graphs' label.

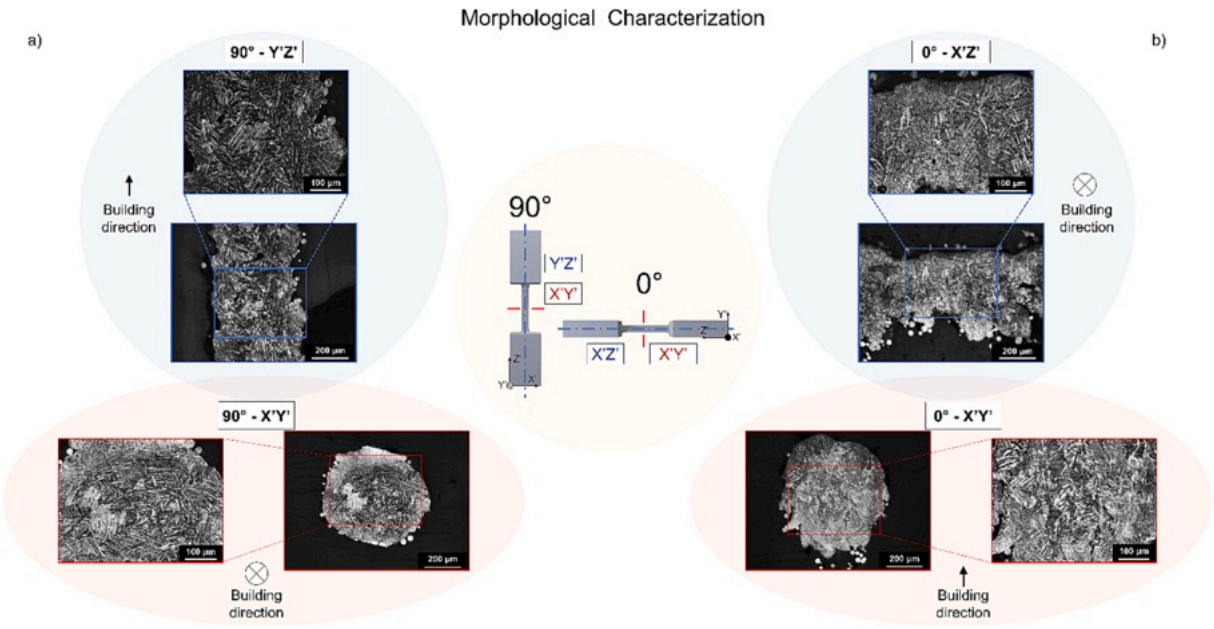

Fig. 5. A) 90° and 0° b) thin-strut microstructural images according to two different investigated sections, namely on the x'y' and y'z' planes for the 90° specimen and x'y' and x'z' for the 0° specimen. the scale bar is set at 200 μm for the larger images and at 100 μm for the close-up images.

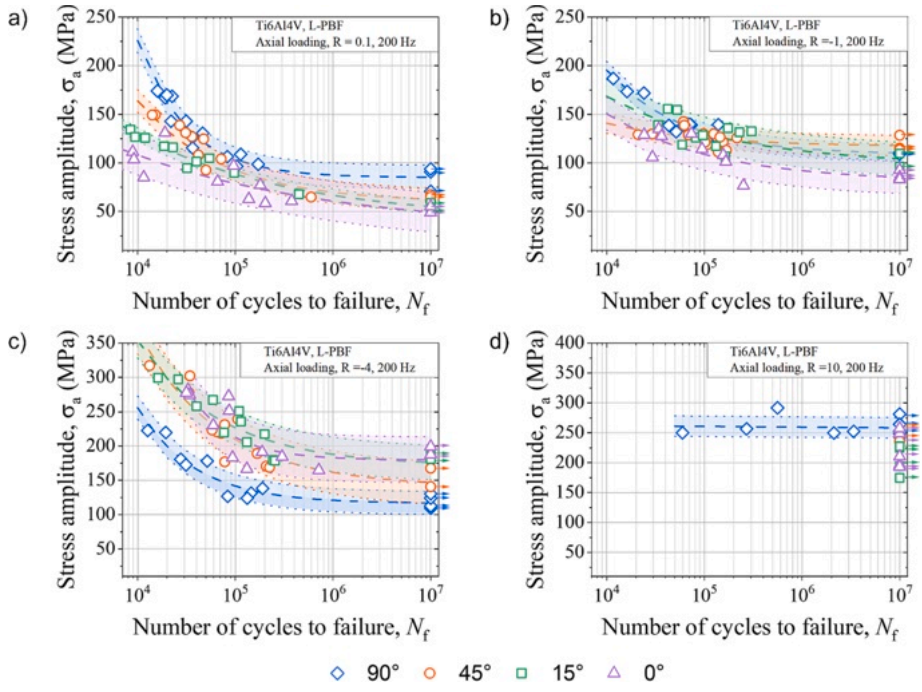

Fig. 6. S-N fatigue curves in a semi logarithmic scale calculated at the four different stress ratios, namely R = 0.1 (a), R = -1 (b), R = -4 (c) and R = 10 (d). In each S-N plot the four fatigue curves according to the different orientation of the specimens are reported. In blue the 90° struts, in orange the 45°, in green the 15° and in purple the 0° specimens. Run-out specimens are labelled with a horizontal arrow. Color bands indicate 10 %-90 % failure probability. In Figure (d) only the S-N curve of the 90° specimen is reported. For the other orientations, due to the buckling predominancy, only the runout values are reported.

sectional data only. The rationale behind the author's decision is that fatigue is a highly localized phenomenon, and it can be better depicted by the minimum cross-section rather than the average or nominal one. It is often true that cracks tend to nucleate and propagate in the narrowest valleys of thin-strut specimens where notches act as stress concentration raisers. A better assessment of this phenomenon can be therefore obtained by employing minimum cross-sectional value rather than the average or nominal data. For further considerations on the employed choice, the reader is addressed to [19].

L-PBFed lattice specimens are highly subjected to surface defects as well as internal defectiveness, such as lack of fusions (LoF) and gas holes [57,58]. As reported in *Section 3.1*, defects are intrinsically linked to the manufacturing process and the building orientation of the manufactured specimen. It is thus trivial to state that the printing direction strongly impacts the overall fatigue strength of AM components.

Tension-tension (R = 0.1, Fig. 6a) S-N curves clearly show the fatigue life dependency on the building orientation effect. 90° thin struts exhibit the highest fatigue strength either in the low cycle (LCF), with a $\sigma_{a,50\%}$

$_{@10}^{4}$ of 226 MPa, and high cycle (HCF) fatigue regime, $\sigma^{7}_{a,50\%@10}$ of 85 MPa, as reported in Table 2. Conversely, 0° specimens report the lowest values in the entire tested range, respectively at 108 MPa and 49 MPa. A clear trend is hence evincible: the lower the printing angle is, the lower the fatigue strength is. It is therefore understandable that, in a tension–tension regime, the fatigue strength of thin struts is driven by the surface texture quality of the specimens, hence reflecting the trend of increasing roughness with a decrease of building angle, reported in our previous work on miniaturized specimens manufactured with the same process parameters herein involved [19].

Moving towards the R = −1 tension–compression fatigue regime (Fig. 6b), the building orientation effect varies, and the previously described trend is only partially noticeable. 0° thin strut specimens still report the lowest fatigue life in HCF ($\sigma^{7}_{a,50\%@10}$ of 85 MPa). Additionally, a wider discrepancy to the other group of three curves is registered. Conversely, 90° specimens do not exhibit anymore the highest fatigue life in HCF ($\sigma^{7}_{a,50\%@10}$ of 110 MPa), instead shown by 45° ($\sigma^{7}_{a,50\%@10}$ of 118 MPa) specimens. In the LCF, 90° struts still manifest the highest fatigue strength among the four batches (with a $\sigma^{4}_{a,50\%@10}$ of 195 MPa), followed by 15°, 0° and lastly 45° printed specimens, as noticeable in Table 2. Differently from the tension–tension regime, the sensitivity to surface defects seems to not be the only main driving mechanism ruling out the fatigue strength of the components. We indeed believe that the role of porosity needs to be also accounted for. As a matter of fact, the decrease in fatigue life of vertical specimens, if compared to the other three batches, might be ascribable to the presence of larger inner defects, i.e., LoF and gas holes [19]. We, therefore, hypothesize a synergistic failure mechanism, where surface defects and porosity simultaneously impact the fatigue resistance of the printed specimens. Nevertheless, if this might hold true for vertical specimens, it does not seem the case for inclined specimens. In the latter, failure mechanisms induced by surface defectiveness are still predominant, as further and deeper discussed in *Section 3.3.3*.

Moving to the R = −4 condition (Fig. 6c), where the compressive state (75 %) is higher than the tensile (25 %) one, another different trend for the building orientation can be appreciated. Interestingly, for this stress ratio, the building orientation effect is opposite to the R = 0.1 case. 90° thin struts report the lowest fatigue life of 117 MPa at runout, with a negative relative difference of about 20 % from the 45° and 35 % from the 15° and 0° specimens. This change in the printing orientation trend can be again correlated to the beneficial effect of compressive states in slowing down the nucleation and propagation of surface cracks, with a higher effect of the internal defects, typical of 90° and, to some extent, of 45° specimens. The further decrease shown by the 90° specimen fatigue life might suggest a further predominancy of a leading role of inner porosity, if compared to the other three orientations.

The pure compression-compression regime (R = 10) is instead reported in Fig. 6d. In this case, only the fatigue curve at 90° could be built, while for the other orientations only values at 10^7 cycles were calculated. This can be ascribed to the specimen's tendency to either undergo buckling instability after a few compressive cycles or going to run out. The only specimens able to undergo fatigue failure are the vertical thin-struts, which also report the highest critical buckling stress and better printing accuracy. A better representation of the fatigue life at 10^7 cycles is instead reported in Fig. 7. In these graphs, the buckling onset bands are also reported as stress amplitude values, where the critical buckling stress in considered the σ_{max} of the compression-compression fatigue regime. Interestingly, the miniaturized specimens exhibit a similar building orientation trend described for R = 0.1 specimens, where a decrease in the fatigue life is associated with a decrease in the printing angle. Despite a similar trend to the R = −4 might be expected, the higher pure compressive loads can often lead to buckling instabilities before the fatigue failure. Consequently, this phenomenon and its driving factors need to be addressed to have a better insight into the building orientation effect at R = 10. A discussion on buckling is reported in the following section (see *Section 3.3.2* and *Section 3.4*).

3.3.2. Influence of the stress ratio

Comparing the data reported in Table 2 and Fig. 6a-d, the influence of the stress ratio on the fatigue properties of the specimens is evident. An increase in the fatigue strength of the specimens at 10^7 cycles is recorded moving from cyclic tensile to compressive fatigue regimes. This holds for all four batches and is in line with other recently published works, where the fatigue life of AM Ti-6Al-4V specimens at different stress ratios was investigated [39,41,59]. Tensile cyclic loads are usually accelerators of the fatigue failure of the specimens, due to the opening effect that these stresses have on cracks, leading to multiple crack initiation sites on the outermost as-built surfaces of lattice struts. On the other hand, closing compressive normal stresses can act as partial inhibitors of crack propagation, thus increasing the fatigue life of the specimens. Despite multiple cracks can still be generated from the surface, internal defects and residual stresses become more influential factors for the fatigue failure of the component [59].

To sum up the influence of the stress ratio and the building

Table 2
Fatigue fitting coefficients (C1, C2, C3) and mean square errors are reported for each orientation at each stress ratio. The stress amplitude at 50 % failure probability for four given cycles (10^4, 10^5, 10^6, 10^7) are then reported. For the R = 10 loading conditions, no curves were obtained and only average run out values are reported.

		C1	*C2*	*C3*	*MSE*	$\sigma^{4}_{a,50\%\ @10}$ *(MPa)*	$\sigma^{5}_{a,50\%\ @10}$ *(MPa)*	$\sigma^{6}_{a,50\%\ @10}$ *(MPa)*	$\sigma^{7}_{a,50\%\ @10}$ *(MPa)*
R = 0.1	***90°***	85	436,932	0.87	88	226	104	87	85
	45°	59	10,254	0.49	82	164	92	70	63
	15°	42	1064	0.27	27	129	88	67	55
	0°	30	508	0.20	253	108	79	61	49
R = -1	***90°***	109	17,011	0.57	*50*	195	132	115	110
	45°	117	1342	0.44	66	141	126	120	118
	15°	97	1556	0.33	177	169	130	112	104
	0°	81	2638	0.39	170	151	109	92	85
R = -4	***90°***	116	127,419	0.74	173	256	142	121	117
	45°	140	25,298	0.51	591	365	210	162	147
	15°	171	208,440	0.51	384	354	227	188	176
	0°	180	3,160,596	0.99	681	508	213	183	180
R = 10	***90°***	171	97	0.0061	177	–	261	260	258
	45°	–	–	–	–	–	–	–	245
	15°	–	–	–	–	–	–	–	205
	0°	–	–	–	–	–	–	–	221

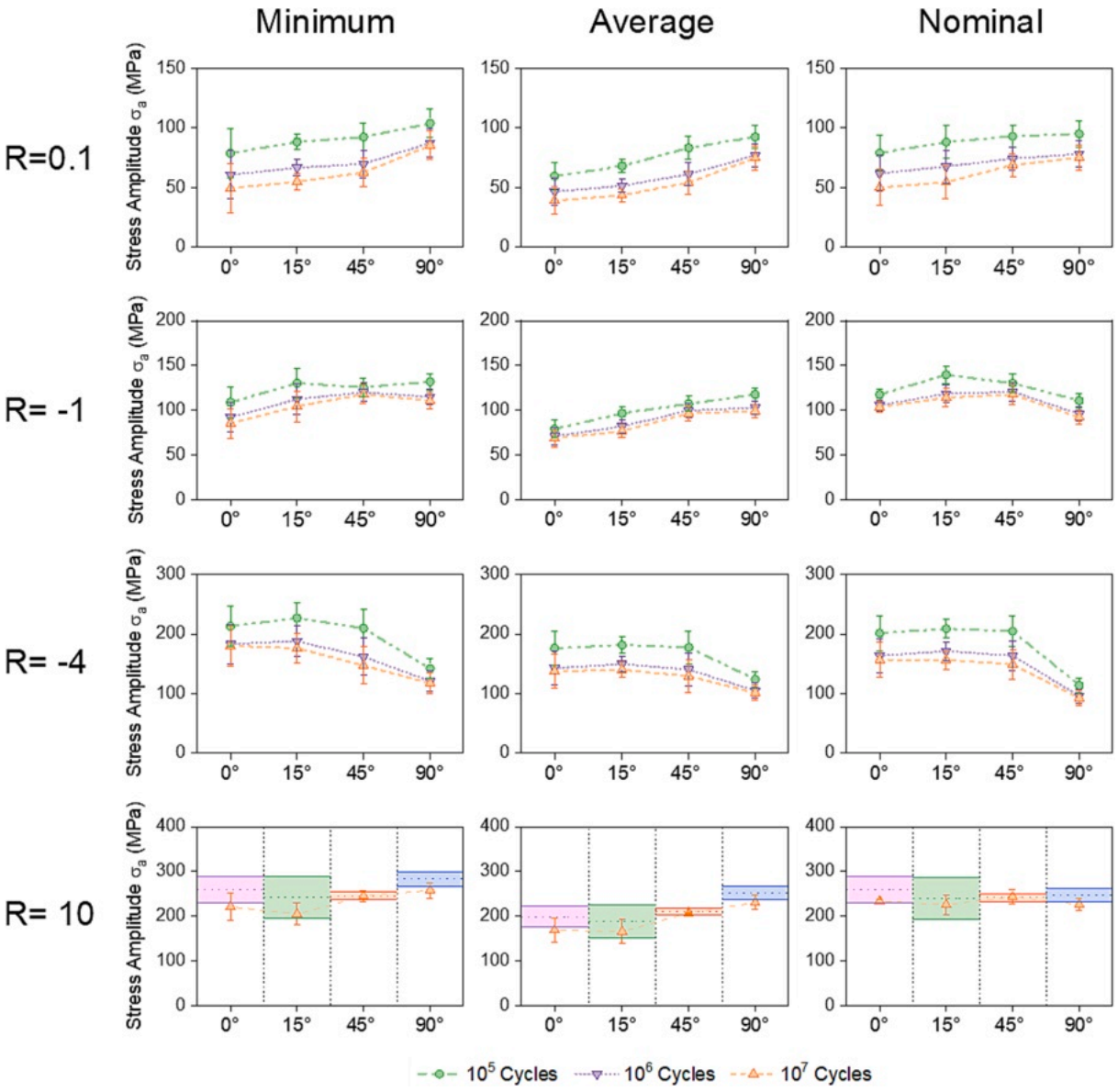

Fig. 7. Stress amplitude trends as function of the building angles are reported for given cycles at each stress ratio. In green the 10^5 cycles, in purple the 10^6 and in orange the 10^7 cycles level. Stress amplitude value are to be considered at 50 % failure probability. Errors are also reporting representing the 10 %-90 % failure scatter bands. For R = -10, only the stress amplitude at 10^7 cycles is reported. The colored bands in R = 10 graphs represent the buckling onset (dotted line mean critical buckling stress). For all the four investigated stress ratios, data obtained with minimum, average, and nominal cross-section were considered.

orientation effect at different fatigue cycles, comparative charts are reported in Fig. 7. Data related to the nominal and average cross-sections are also depicted and similar trends to the above-mentioned can be noticed. An increase in the fatigue life with the increase of compressive stresses, as well as similar building orientation effects according to each investigated stress ratio can be indeed detected. It is however worth noting that for R = −81, a less pronounced effect on the HCF of 90° thin struts is manifested. This holds particularly true for the fatigue data based on the average cross-section, which appears to be less sensitive to the 90° building orientation effect changes. Nevertheless, moving to the R = -4 loading condition, identical trends among the different involved cross-sections are restored.

For pure compressive stress ratio (R = 10), the fatigue values at 10^7 cycles are graphed together with the buckling critical stress per each building orientation. The critical buckling stresses (dotted lines) were calculated averaging the critical buckling load stress (c = 0.5, see Table 4) over the entire number of specimens of each batch. These values are reported along with their standard deviation (colored filled regions) in Fig. 7. The author's decision behind choosing the most critical *c* coefficient lies in the more accurate prediction of the buckling onset. Hence, the fatigue limit in a compression-compression regime never exceeds the predicted buckling regime, falling within the lower part of the buckling range or even below it, i.e., 90° and 0° thin struts. Within this context and being aware that further and more in-depth analysis should be conducted, it is possible to suggest the lower threshold of the critical buckling stress band can be adopted as an enough conservative reference to determine the buckling onset of thin strut specimens.

Additionally, similar trends can be appreciated by adopting the average cross-sections, either in terms of the fatigue life versus the building orientation trend or of fatigue versus buckling onset. Nominal cross-sections report a lower sensitivity to the building orientation effect, with a more uniform behavior for all the four specimen batches.

3.3.3. Influence of porosity and surface texture: Fatigue failure mechanisms and CT scans

Fig. 8a-d depict some Example SEM images of the fatigue failure surfaces of the various specimens, according to the different building orientations and stress ratios. In the tension–tension fatigue regime (R = 0.1), cracks always nucleate and propagate from micro-notches or irregularities present on the specimen surfaces. This is particularly evident for inclined, viz. the 45° batch, or horizontal specimens, viz. the 0° batch, where partially melted particles do not properly fuse together, thus generating a sharp notch at their conjunction. The latter phenomenon leads to a local stress concentration, detrimentally impacting the fatigue strength of the specimen. It is worth noting that for inclined and horizontal specimens the crack onset typically appears on the sample lowerskin, due to the higher texture and surface defects. A larger amount of unmolten or partially melted powder particles populate the specimen lowerskin. Multiple cracks can also nucleate from different surface locations and propagate on different paths till their convergence. This is particularly clear for the 45° specimen reported in Fig. 8a, and graphically sketched in Fig. 9a. Additionally, it is worth noting that dimples, indicating the fatigue overload and final failure stage of the component, are generally located in the upper skin of the specimens. Moreover, the four batches of thin struts examined do not exhibit significant internal defects on their fatigue failure surfaces. This finding confirms that fatigue-driving factors for the investigated stress ratio mainly stem from surface irregularities rather than internal defectiveness.

As described in the previous sections, the introduction of a compressive phase in the fatigue regime beneficially impacts the overall fatigue properties of the thin struts. Nevertheless, in the case of a fully reversible fatigue cycle (R = −1), any difference is evident with respect to the failure mechanisms described for the R = 0.1 condition. The crack nucleation and propagation are still mainly ascribable to the surface defects, especially for inclined and horizontal specimens. 90° specimens show however pores on the failure surface, although not being "active" paths of the crack propagation. Nevertheless, when the compressive load becomes predominant in the fatigue cycle (R = −4, 75 % compressive loads), different outcomes can be pointed out. Investigating the failure surfaces of 90° and in part 45° specimens (Fig. 8c), it is indeed possible to highlight how cracks nucleate and, to a major extent, propagate from internal defects, usually located in the surface proximities. It is also worth noting that several cracks depart perpendicularly to the layer thickness ridges in multiple areas of the gauge length. Conversely, lower inclined struts do not report any evident internal defect on the inspected surfaces. These outcomes might confirm the different fatigue behavior of the 90° specimens in a predominantly compressive cyclic regime and might be explanatory of the previously discussed trend inversion of the building orientation effect.

Fig. 8d reports the failure surfaces of the 90° specimens at R = 10, which are the only specimens undergoing a fatigue failure in a pure compressive regime. The inspection of the failed cross-section again reveals the presence of pores from which cracks nucleate and propagates, as for the R = −4 counterparts. Interestingly, several cracks can be noticed along the gauge length, propagating parallel to the layer thickness ridges, as clearly visible in Fig. 8d. Concluding, the authors believe that different driving factors can affect the fatigue failure mechanisms according to the combination of stress ratio and building orientation of the AM printed specimen.

In Fig. 9*a-d, a* series of sketches is presented to summarize the main driving factors influencing the fatigue failure mechanisms based on the combination of stress ratio and building orientation of the AM printed specimen. The sketches illustrate the following *(i)* for low-inclined

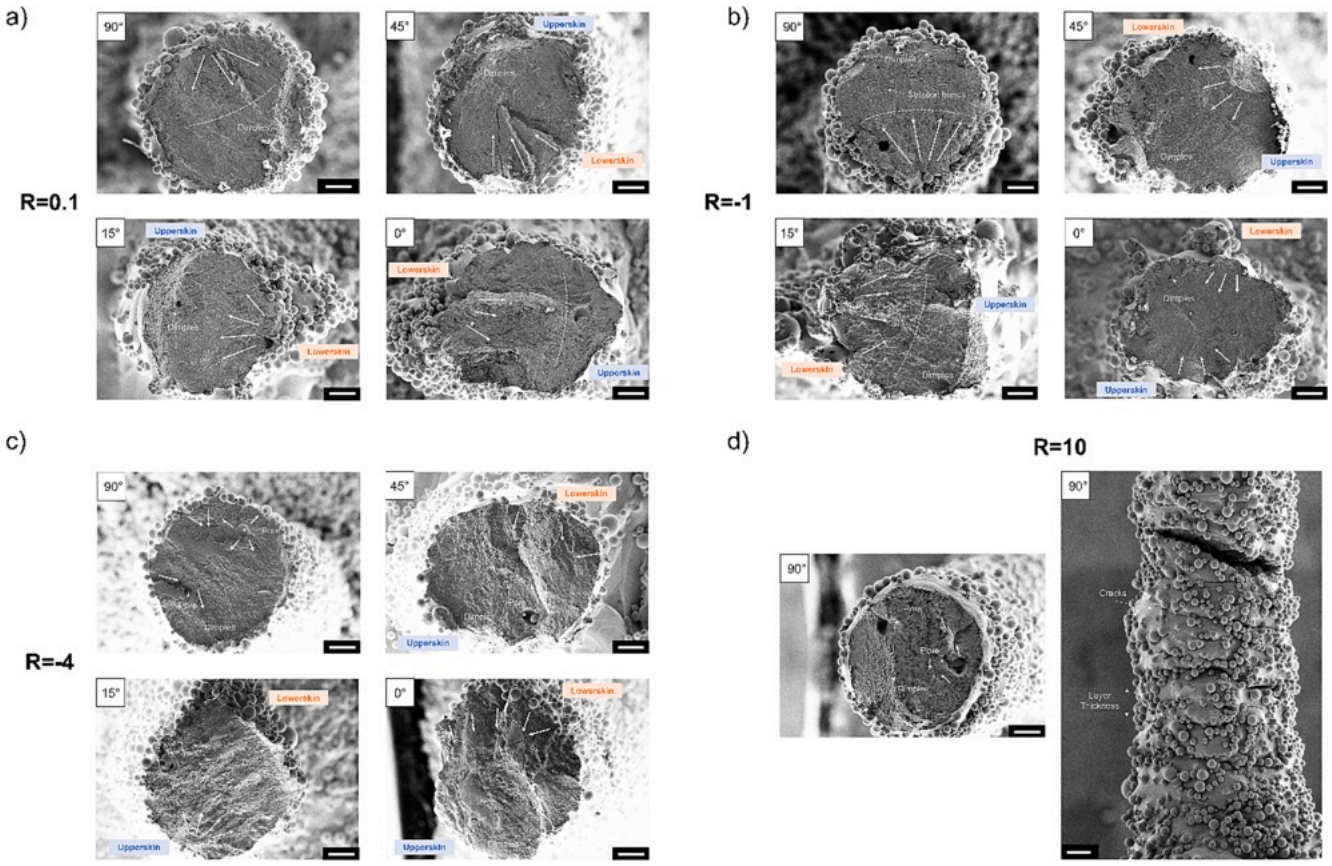

Fig. 8. Example SEM fracture images reported the fatigue-failed specimens are reported for the four building orientations, considering a) R = 0.1, b) R = -1 and c) R = -4 d) R = 10 loading conditions. For each image labels indicating the upper and lowerskin of the specimens along with the crack onset and propagation and the presence of dimples and pores are reported. Scale bars are set to 100 μm.

specimens across all stress ratios, surface texture defects are the primary driving factor leading to fatigue failure. Cracks often propagates due to partially melted particles, high surface texture and cross-sectional variations which act as stress concentration sites. This mostly occurs in the lowerskin of the specimens. In support of this, Fig. 9e reports an Example CT scan image of a partially propagated crack (in red) over the specimen transparent view. This shows that the crack in this case is not correlated to pores and does not correlate to the largest surface depression in the

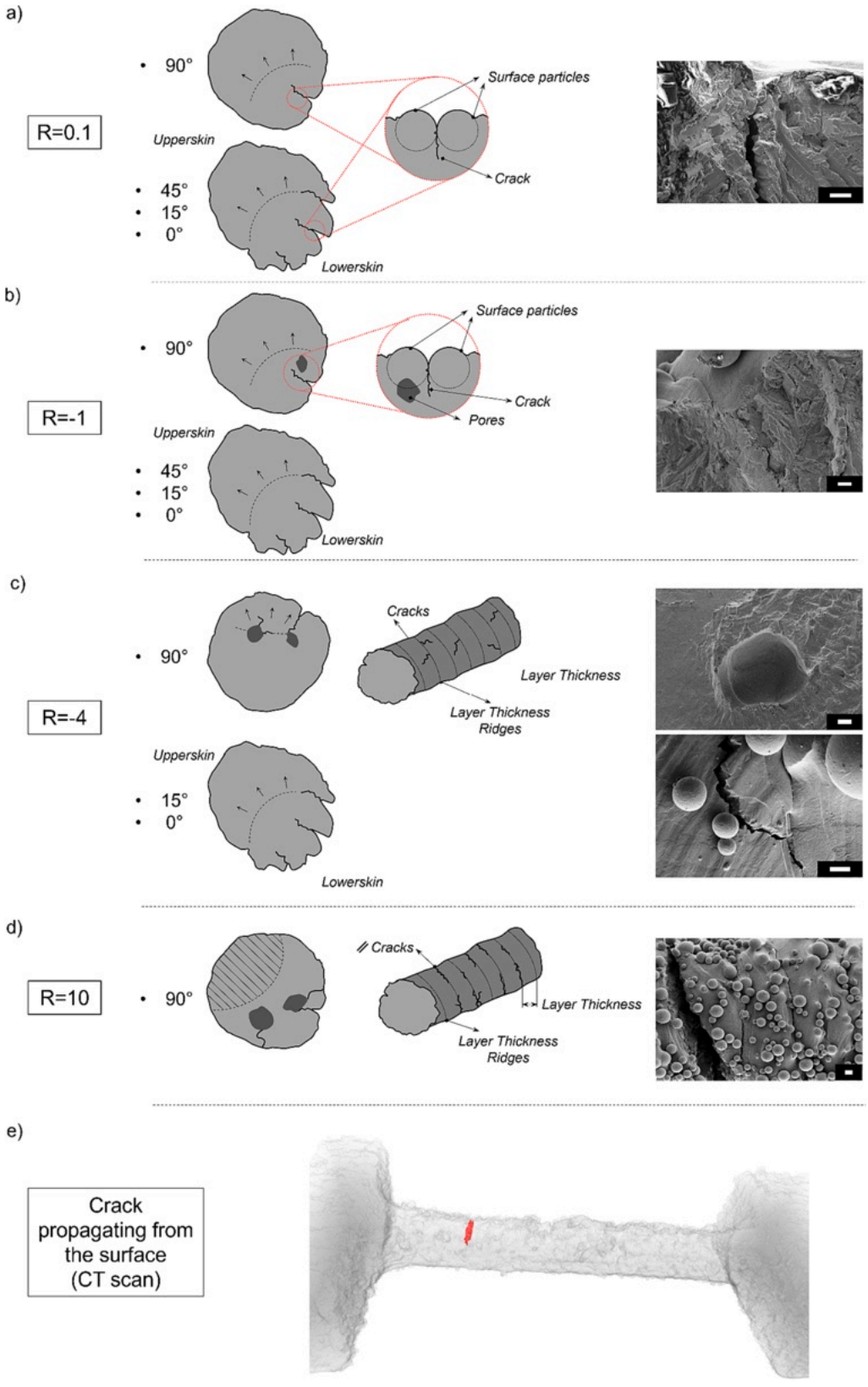

(caption on next page)

Fig. 9. Example sketches of the possible fatigue failure mechanisms for each building orientation and at each different stress ratio. Different SEM close up images of typical defects associated to the failures are reported for each sketch. a) In a tension–tension fatigue regime (R = 0.1), surface defects are the driving nucleation site of cracks, which usually propagate from the lowerskin of the specimens, also from multiple different sites. The associated SEM image indicates the formation of a notch from particles which did not properly sinter. The scale bar is set to 10 μm. b) In a R = -1 fatigue regime, the mechanism is similar to the R = 0.1 for inclined and horizontal specimens. In this case an example SEM image of a crack propagating due to cross-sectional variations is reported. The scale bar is set to 10 μm. Vertical specimens instead report pores close to the crack initiation site, despite not being "active" in the crack nucleation or propagation. c) When the compressive loads are predominantly in the fatigue regime, i.e., R = -4, pores take an active role in the crack nucleation or propagation path. This holds true for 90° specimens, while for the other inclinations the propagation mechanisms is unchanged. An example SEM image of propagating cracks in the proximity of a pore are found in vertical strut fatigue failure surfaces. The scale bar is set to 10 μm. Vertical specimens also report cracks propagating in between layer thickness ridges along the specimen gauge length, as reported in the second SEM image. The scale bar is set to 10 μm. d) In a pure compression-compression fatigue regime (R = 10), only vertical specimens failed under fatigue, with a mechanism comparable to the one reported for R = -4 vertical specimens. Interestingly, cracks propagating along the gauge length appears to be more parallel to the layer thickness ridges. The associated SEM image shows a gauge length close up with the propagating cracks. The scale bar is set to 20 μm. e) Example CT image reporting a crack propagating from the outermost lowerskin surface for a specimen printed at 0°.

gauge length, but it originates on the surface of the down-skin surface with roughest surface and a *supplementary video* is provided of this sample. *(ii)* In the case of vertical specimens under tension–tension loading, surface defects continue to play a dominant role in driving fatigue failure, in a similar way to *(i)*. *(iii)* In the case of vertical specimens, the introduction of compressive loads leads to a more remarkable effect of the sub-surface and internal defectiveness. *(iv)* This holds particularly true when the compressive load is the predominant load in the fatigue cycle. Within this context, porosity becomes the driving factor for fatigue failure in vertical specimens.

If the occurrence of fatigue failure is attributed to internal flaws and the presence of pores, the most critical defect should be in principle responsible for the failure mechanism. To verify this hypothesis, the influence of pores was investigated using the statistical of extremes approach as outlined in *Section 2.2.5*. The current statistical analysis is based on two important assumptions and simplifications. Firstly, a constant density of defects was assumed, and secondly, a comparable distribution of defects between the CT-scanned samples and other specimens fabricated with the same printing direction was considered. Fig. 10a shows the two selected volume of analysis, namely the entire gauge length volume of the specimen (V_{POT}) and a surface volume V_s (labeled in dark orange in Fig. 10a). Further details on the selection of these volumes were previously discussed in *Section 2.2.5*. Fig. 10b-e reports the heat map plots according to the four building orientations,

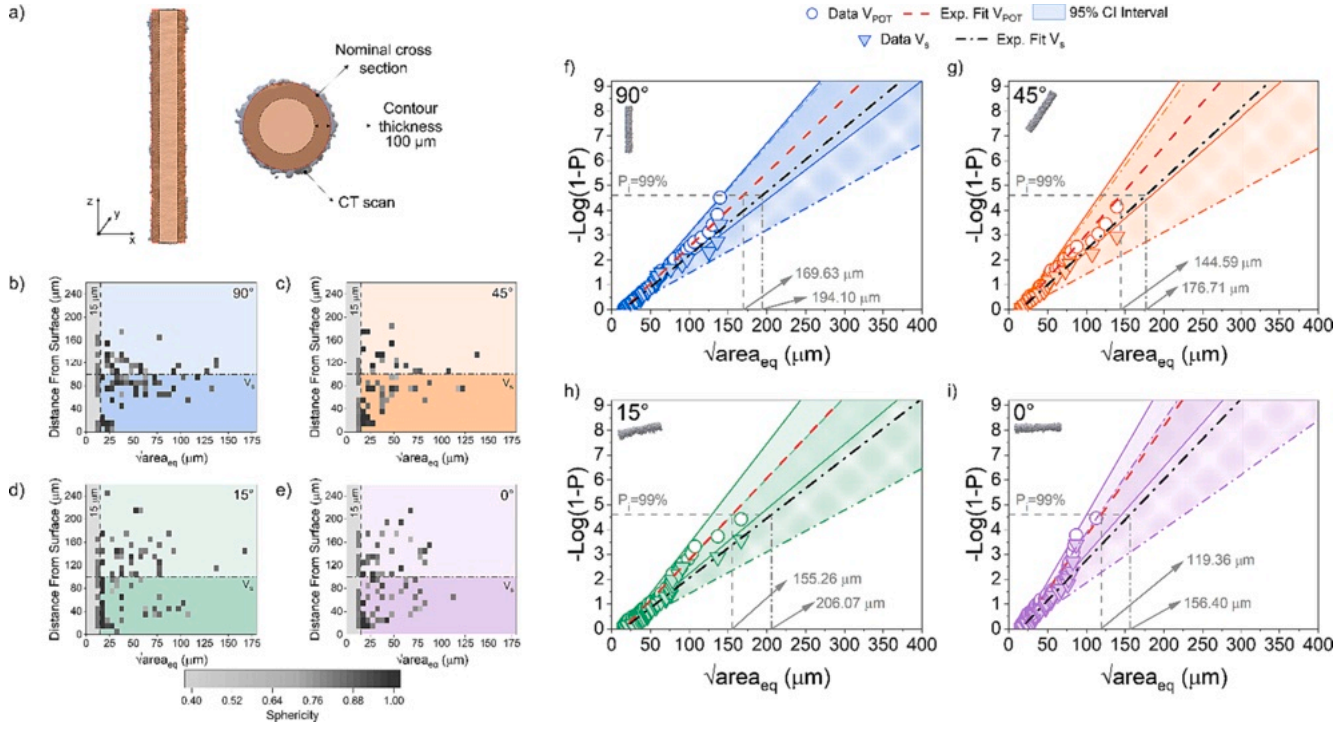

Fig. 10. A) example sketches of the volume of investigations for the defect analysis. two different volumes are chosen, v_{POT} and V_s. V_{POT} refers to the entire CT scan volume, while V_s is the toroidal surface volume represented in dark orange. The thickness of the circular crown is of 100 μm, thus similar to the contour scanning thickness employed in the printing strategy. Figure b) to e) report the heat map plots correlating the defect size, through the Murakami area, $\sqrt{area_{eq}}$, on the x axis, with the distance from surface on the y axis and the sphericity as a continuous variable ranging from 0 to 1. The latter is associated to a colour scale bar, where 1 corresponds to black and zero to white. Two different threshold lines are also visible in the four graphs. A vertical dashed line set at $\sqrt{area_{eq}}$ equal to 15 μm and a dash-dot line set at 100 μm of distance from the surface. The first is the u threshold of the POT approach, while the second helps delimiting the toroidal surface volume V_s. This volume is further highlighted by the darker color associated to each building orientation, thus blue for 90° (9b), orange for 45° (9c), green for 15° (9d) and pink for 0° (9e). Figures f) to i) report the defect distribution of the exceedances in a negative exponential probability plot. The threshold u is set fixed at 15 μm. The statistical analysis has been performed for the two different volume of interest and plotted together in each graph. The red exponential fitting line (associated to the white circle markers indicating the experimental data) refers to V_{POT}. 95 % confidence interval bands are also reported and visually represented by the full filled color. The black dot-dash line refers to the exponential fitting line for the V_s analysis. Full down-facing triangle markers are the associated experimental values, while the checkboard-like patterned area depicts the associated 95 % confidence interval. Also, for these plots the colours are distinguished according to each building orientation, namely blue for 90° (9f), orange for 45° (9 g), green for 15° (9 h) and pink for 0° (9i).

depicting the CT-detected defects with respect to their size, $\sqrt{area_{eq}}$, minimum distance from the surface and sphericity, where 1 refers to a perfect sphere (black). Data laying in the grey area are cut off the statistical analysis, falling below the selected threshold u of 15 μm. Data laying into the two different volumes of inspections are also visually represented. Particularly, V_s data are defined by the darker color region associated to each building orientation and by a horizontal dash-dot threshold line at 100 μm of distance from the surface. From a visual inspection of Fig. 10b-e, it is possible to notice that vertical specimens, and partially 15°, reports a larger number of defects of higher dimensions in comparison to the other two batch of specimens. Focusing on the sphericity, lower inclined specimens seem to report values further departing from the perfectly spherical pores, in comparison with vertical components. This might suggest that defects generated in 90° specimens can be mainly associated to gas holes, rather than LoFs. Nonetheless, for all four batches, sphericity is reported to be higher for lower values of $\sqrt{area_{eq}}$, while decreasing with an increase in the pore size.

Fig. 10f-I reports the defect distribution in a negative exponential probability plot, fitting the exponential distribution of exceedances above the threshold u, for the two volumes of investigation, viz. V_{POT} and V_s. Experimental data associated to V_{POT} (circle white markers) and to V_s (downfacing colored triangle markers) are plotted along with the exponential fitting line (red dashed line for V_{POT} and black dash-dot line for V_s). Additionally, the associated 95 % confidence interval bands are reported for both analysis (full colors for the V_{POT} and patterned color for V_s). The maximum defect size associated with a cumulative probability P_i of 99 % is reported for V_{POT} and V_s, in Fig. 10f-l and Table 3. As noticeable, the highest value of $\sqrt{area_{eq.Max}}$ for the entire volume of scan is found for 90° specimens (194.10 μm), while the lowest is encountered for horizontal specimens (119.36 μm). No specific trend according to the building orientation can be detected, since 15° oriented struts report a highest $\sqrt{area_{eq.Max}}$ with respect to 45° oriented specimens (namely of 155.26 μm and 144.59 μm). All specimens report experimentally detected pores close to the predicted $\sqrt{area_{eq.Max}}$, thus suggesting that possible internal "killer" defects can be found at every building orientation. Nonetheless, solely considering the pore size might not be sufficient to define a defect as "killer". It is indeed well-known that the distance from surface and the defect morphology are further factors that cannot be excluded. Surface volume V_s allows the investigation of the role of subsurface defects which are populating the contour scanning area of the cylindrical cross-section of the specimens. Interestingly, it is possible to notice that the four batches systematically report $\sqrt{area_{eq.Max}}$ defects with a larger size than the previously reported data. This might be ascribable to a greater number of defects of larger size in proximity of the outermost surface rather than in the central part of the strut [30]. Considering the $\sqrt{area_{eq.Max}}$ in V_s according to each building orientation, 15° (206.07 μm) and 90°(194.10 μm) specimens still report the highest values if compared to the 45° and 0° struts (176.71 μm and 156.40 μm). Furthermore, looking at the total porosity over the scanned volume reported in Table 3, 90° specimen exhibits the highest porosity percentage (0.206 %), in line with similar analysis of L-PBF Ti6Al4V thin strut specimens printed with the same process parameters [19]. This data combined with a relevant high number of defects with $P_i > 90$ % in comparison with the other building orientations might be of further support to explain the failing mechanisms of vertical specimens under a major compressive fatigue regime. These specimens might be more prominent to undergo failure due to porosity rather than the other three inspected building orientations. It is also worth noting that vertical specimens suffers of lower surface irregularities than 15° specimens, as reported in [19]. This might explain why pores are not reported on the SEM fracture surfaces of the latter batch of specimen. The authors leave for future work the surface roughness measurements through CT scans and the synergistic interaction of the latter with internal defects. Particularly, the role of surface micro-notches, through their consideration as defects projected on the axial plane, via the $\sqrt{area_{xy}}$ parameter, should be assessed and integrated into the reported analysis. The employment of statistic of extremes approaches and machine learning methodologies towards strategies for the strut fatigue life prediction should be considered, as already reported in [60,61].

Table 3
CT scan summary data of the porosity percentage, volumes of investigation (V_{POT} and V_s) and critical defect size measured through the statistic of extremes exponential distribution at 99% probability.

	Porosity (%)	V_{POT} (μm^3)	V_S (μm^3)	$x_{max,\ VPOT}$ (μm)	$x_{max,\ Vs}$ (μm)
90°	0.206	$1.14 \cdot 10^9$	$9.63 \cdot 10^8$	169.63	194.10
45°	0.088	$1.41 \cdot 10^9$	$1.23 \cdot 10^9$	144.59	176.71
15°	0.120	$1.65 \cdot 10^9$	$1.46 \cdot 10^9$	155.26	206.07
0°	0.062	$1.64 \cdot 10^9$	$1.44 \cdot 10^9$	119.36	156.40

3.4. Monotonic properties and buckling behavior

The understanding of fatigue behavior of thin strut specimens hinges on the crucial assessment of monotonic and buckling properties. However, this section is peripheral to the core focus of this work, which primarily revolves around the fatigue assessment of miniaturized specimens, and its primary purpose is to provide the necessary information for defining the Haigh diagrams. As a result, only a concise discussion of monotonic properties is presented herein. Further elucidation on this topic is however available in *Table S2* and *Figure S1* in the *Supplementary Material*. Table 4 conveniently summarizes the principal monotonic properties, which were subsequently used in the calculations of the mean stress predictive models as detailed in *Section 2.2.3*.

Notably, the stresses were calculated by considering the average cross-section of each tested specimen. This approach was chosen to capture these properties in a more representative manner, as it considers the global behavior of the specimens rather than solely focusing on the nominal or minimum cross-sectional area. This consideration is important since tensile and compressive failures of the specimens are often associated with their overall performance rather than the minimum local load-bearing cross-section.

The data in Table 4 are consistent with the findings from previous work on MAM miniaturized specimens [24,25,54,62–65], despite being generally lower than the values obtained from standard-sized AM specimens, particularly those made of wrought Ti6Al4V.

The reasons behind these discrepancies may be attributed to various factors. Different printing and process parameters can influence the microstructure and morphology of AM component, especially in the case of small-scale specimens. AM components are often associated to a low reproducibility and scatter in the component geometry, which can lead

Table 4
Main parameters calculated from the monotonic tests, in tension and compression. Reported data are employed for the mean stress predictive model calculations and the critical buckling stresses. The latter, herein reported, refers to a coefficient c = 0.5. Data are reported as mean values along with their standard deviations for the four inspected orientations.

	Tension		*Compression*		*Buckling*	
	Yield strength σ_y (MPa)	Ultimate strength σ_{UTS} (MPa)	Yield strength σ_{cy} (MPa)	Ultimate strength σ_{UCS} (MPa)	P_{cr}(N)	σ_{cr}(MPa)
90°	657 ± 19	816 ± 5	630 ± 44	766 ± 47	194 ± 11	602 ± 41
45°	523 ± 71	609 ± 89	486 ± 22	669 ± 23	189 ± 7	470 ± 21
15°	532 ± 29	636 ± 11	492 ± 78	589 ± 42	188 ± 36	474 ± 74
0°	633 ± 86	812 ± 17	514 ± 16	592 ± 11	204 ± 23	495 ± 14

to severe fluctuations in mechanical properties. These fluctuations are closely related to the size, printing strategy, and geometrical quality of the specimen. In contrast, traditional subtractive manufacturing techniques tend to exhibit a higher degree of reproducibility and lower geometric-induced material anisotropy. The size effect plays another significant role in the mechanical outcomes of AM components. When dealing with miniaturized specimens, such as those in the mm/sub-mm scale, the high surface-to-volume ratio must be factored in. Defects, in this case, have a stronger impact on the overall mechanical properties of the component, as for instance reported by *Phutela et al.* [54] on L-PBF Ti6Al4V specimens of similar dimensions. Mixed-mode stress fields can indeed be generated due to unwanted local curvatures or gauge length twists. For specimens tested in compression, this can lead to buckling instabilities, where not only pure compressive loads but also eccentricity-induced bending moments can arise [47]. Furthermore, the definition of the real load-bearing section is still unclear. Parasitic masses and unmolten surface particles are a non-load bearing yet significant section of sub-mm struts, which detrimentally impact on the calculation of the specimen's strength and elastic modulus [24,63].

Furthermore, it is worth noting that uniaxial testing may not be the most accurate approach for miniaturized specimens due to their unique design, as pointed out by *Zhang et al.* [26]. They suggest that uniaxial testing often results in underestimating the elastic modulus, although it can provide reliable measurements for yield and ultimate tensile strength. This observation is also consistent with our previous research [19], where we compared the testing method used here with DIC (Digital Image Correlation) measurements on identical miniaturized 45° thin strut specimens. We conducted these tests using an in-situ scanning electron microscope (SEM) equipped with a tensile module. Our findings indicated a reasonable level of agreement between the two measurement techniques, particularly for yield and ultimate tensile strength, thus demonstrating the feasibility of the chosen testing methodology.

As previously mentioned, struts can experience buckling instabilities when subjected to compressive loading. When the stress amplitude in the fatigue regime surpasses the critical buckling stress, it can lead to premature buckling rather than fatigue-induced failure mechanisms. Therefore, predicting the critical buckling load is of paramount importance, especially in the context of lattice strut elements.

We calculated the critical loads and associated stresses using *Eq. (1)* from *Section 2.2.2*, considering the experimental yield strength reported in Table 4. Buckling critical loads and stresses are also outlined in Table 4, for a coefficient c = 0.5 (see *Table S3* for c = 0.65). Notably, these data consistently fall below the yield strength, with an average discrepancy of approximately 100 MPa for the 90° and 45° specimens and around 160 MPa for the 15° and 0° specimens. This observed discrepancy is intrinsic to Johnson's formula, as the yield strength represents the highest achievable value. The rationale for adopting the Johnson-Euler approach is that the slender ratio of the thin struts consistently remains below the critical ratio at which the Euler approach can be employed (*viz.* short columns). Under these circumstances, predicting the critical buckling stress using the Euler approach would result in an unrealistic overestimation of the critical stress, as also reported in [47].

However, it is worth noting that the Johnson approach may still lead to a possible overestimation of the critical buckling stress since it does not fully consider the as-manufactured geometry of AM struts. As-manufactured surface texture can lead to an eccentricity-induced shift of the load from the loading axis. This phenomenon should be considered for a more precise buckling assessment of thin struts, as reported by *Alghamdi et al.* [47]. Nevertheless, when comparing the Johnson approach presented here with the Secant method adopted in [47], a greater alignment of the data at the given stress ratio can be observed, always falling below the yield strength (conversely to the classic Euler approach). As buckling data should be seen as instrumental in a deeper fatigue investigation, a more comprehensive analysis of buckling in thin struts is beyond the scope of this study and is therefore left for future research.

3.5. The mean stress effect: Haigh diagram

Fig. 11a displays the four Haigh diagrams at HCF associated to the four different group of specimens at the different inspected stress ratios throughout the fatigue campaigns. The Haigh diagrams plots the 10^7 cycles data derived from the fitting according to *Eq. (3)*. Hence, data at 50 % probability along with the 10 %–90 % error band for the four stress ratios R = 0.1, R = –1, R = −4 and R = 10 are reported on a stress amplitude, σ_a -mean stress, σ_m, graph. An additional dashed line reporting the stress ratio R=∞ is added, since it is the threshold below which the maximum stress becomes negative and results in the asymptotic line of the SWT and Walker models reported in *Eq. (4.2)* and *Eq. (4.4)*. The mean stress correlation models discussed in *Section 2.2.3* are reported as labelled in Fig. 11a. As noticeable, the mean stress effect is evident for all four different building orientations. The classical modified-Goodman approach however cannot properly capture the mean stress sensitivity of the fatigue-tested thin-struts, for the entire σ_m range. This approach seems indeed to systematically underestimate the associated stress amplitude σ_a for $\sigma_m < 0$. Nevertheless, for 90° thin-strut specimens, a good agreement between the R = −4 experimental datum and the modified-Goodman approach is reported, with an almost null discrepancy (see Fig. 11c). Additionally, in the $\sigma_m > 0$, only the 90° experimental value at R = 0.1 is within a reasonable range from the modified-Goodman curve (reported error of about +15 %, see Fig. 11c). Nonetheless, a better overall agreement, through the entire mean stress range, is shown by the FKM and to a higher extent also from the Smith-Watson-Topper (SWT) method. The latter seems to be the most accurate criteria applicable in most cases. SWT model is a specific case of the more generalized Walker approach, where the coefficient α (see *Eq. (4.2)* and *Eq. (4.4)* is intentionally kept fixed at 0.5. Considering the Walker approach as a predictive tool for the fatigue properties evaluation, a fitting procedure of the experimental data is required. Despite this approach might not be optimal under a design point of view (due to the need of experimental campaign), guarantees a better predictive capability of the mean stress sensitivity. As a matter of fact, investigating at the percentage errors of the different adopted criteria, graphed in Fig. 11c, Walker method reports the lowest average discrepancy with respect to the different experimental data. It is worth noting that the Walker's fitting procedures as well as the error reported do not include the pure compression-compression fatigue data, being the mechanism more driven by a buckling failure-fatigue run out categorical phenomenon. This can be also appreciated in Fig. 11a, where buckling instabilities have been included within the Haigh diagram. As a matter of fact, the grey areas in these plots show the region where buckling failure can occur and consequently an additional unsafe region for a wise design of these components. These regions have been defined considering the critical buckling onset stresses as shown in *Eq. (10)*:

$$\sigma_{a,eq} = |\sigma_{max} - \sigma_m| = |\sigma_{cr} - \sigma_m| \tag{10}$$

where σ_{cr} is the calculated critical buckling stress minus its standard deviation (see *Section 3.3* and *Section 3.4.2*).

In general, the outcomes of the predictive models are in line with other works conducted on L-PBF as-built Ti-6Al-4V specimens. For instance, in the work of *Benedetti et al.* [39], L-PBF Ti-6Al-4V coupons with different post-processing treatments were fatigue tested at three different stress ratios. The authors claimed a good agreement between the experimental data with the SWT method. Analogously, *Cutolo et al.* [41], who investigated the mean stress sensitivity in a $\sigma_m > 0$ regime, suggested that the exponential Walker's equation with a φ = 0.385 coefficient exhibits a good prediction of the experimental data for as-built parts. The latter method is an extension of the SWT model, with the adoption of a material- and defect-dependent parameter [41]. *Derrick et al.* [40] thoroughly reviewed numerous works on fatigue of

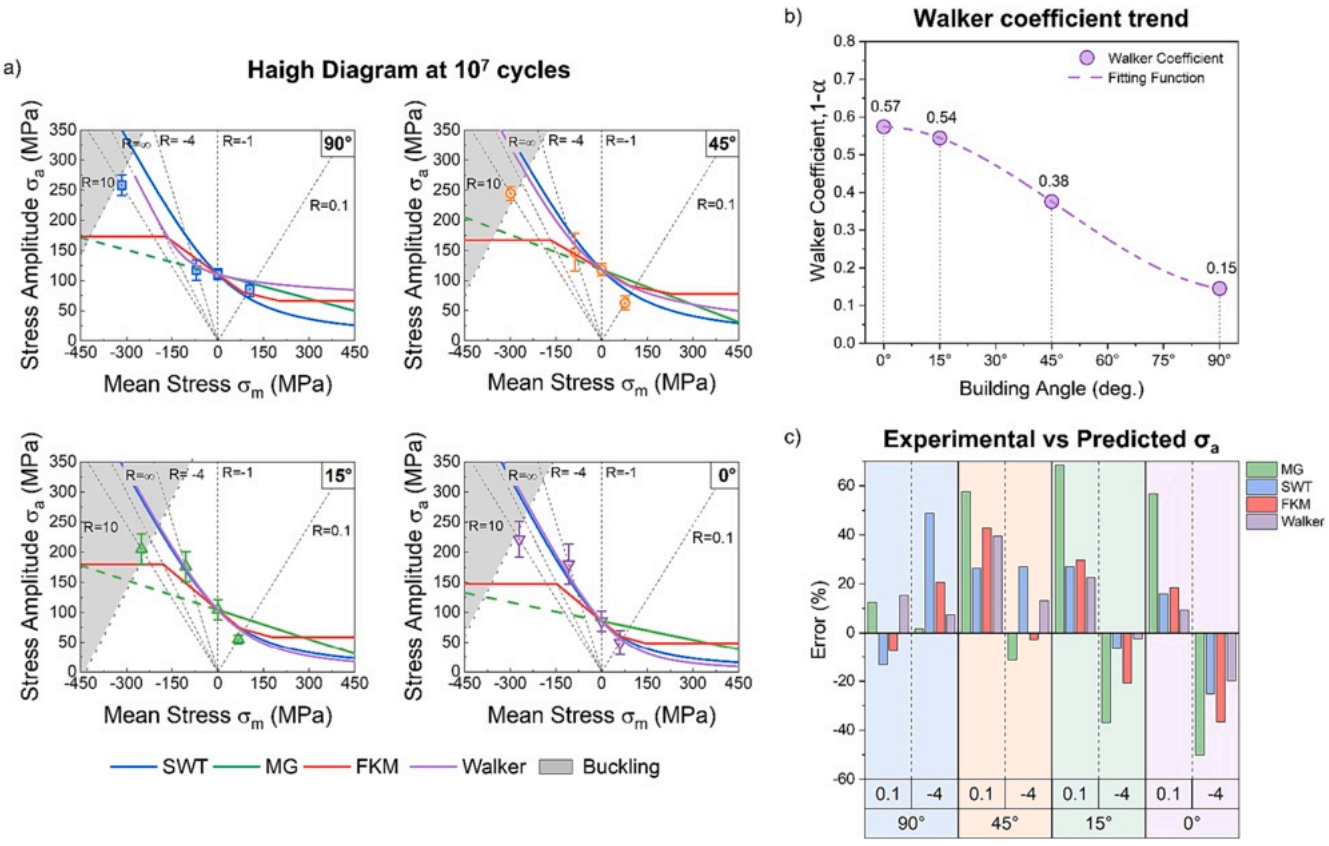

Fig. 11. A) haigh diagram at 10^7 cycles for the four investigated strut orientation. The experimental data are reported with colored markers, specifically blue squares for the 90° data, orange circles for the 45°, green triangles for the 15° and reversed purple triangles for the 0° data. Error bars indicate the 10 %-90 % failure probability for each experimental datum. Dashed black lines refer to the four different stress ratios of experimental interest and the stress ratio R=∞, indicating the transition between positive and negative maximum mean stresses. Modified Goodman (continuous and dashed green line), SWT (blue line), FKM (red line) and Walker (purple line) predictive criteria are superimposed to each Haigh diagram. The grey region of each graph indicates range of possible buckling onset. To account for buckling the lower threshold critical load P_{cr} at c = 0.5 was considered, along with the minimum cross-section averaged over the entire specimen batch. b) Scatter plot of the Walker coefficient over the maximum stress, 1-α, calculated for each building orientation (purple circle markers). A 3rd grade polynomial fitting curve is also represented to visually enhance the inverse trend further with respect to the printing angle. c) Error percentage (%) bar graph of the different predictive criteria from the experimental data. In green the modified-Goodman, in blue the SWT, in red the FKM and in purple the Walker models. The graph is divided according to four colored areas, each for a building orientation, as labelled on the bottom x axis. A further sub-division is made according the two inspected stress ratios, R = 0.1 and R = -4. R = -1 is not shown since the report error is always null, while R = 10 is not shown due to the predominancy of buckling phenomena over fatigue failure mechanisms.

AM metals and particularly as-built L-PBF Ti-6Al-4V at different stress ratios. The authors concluded that the SWT method is a reliable predictive tool in a tensile regime, while when the mean stress is compressive, a higher agreement with the experimental results can be provided by Walker's equation. Within this context and according to our outcomes, it is possible to highlight the importance of the maximum stress on the fatigue properties of the thin struts. Nevertheless, to the author's best knowledge, there is no work in the literature related to the fatigue investigation of Ti-6Al-4V L-PBF specimens according to the building orientation and its effect on the mean stress effect. To address this problem, we decided to investigate the coefficient $1-\alpha$ over the maximum stress in the Walker's equation (*Eq. (4.4)* and correlate it to the building orientation. Interestingly, a decreasing trend of the coefficient with an increase of the building angle is detectable as reported in Fig. 11b. Horizontal and 15° specimens report the highest $1-\alpha$ coefficient (namely of 0.57 and 0.54), setting slightly above the 0.5 coefficient of the SWT model, thus also indicating that the latter model can fit well the experimental data. A higher drop is instead registered for 45° (0.38) and particularly 90° specimens (0.15), showing to be less influenced by the mean stress effect. As reported by *Cutolo et al.* [41], the Walker's coefficient α can be considered as a defect-sensitivity parameter rather than a material-dependent intrinsic property [66]. The authors indeed suggest that this coefficient can be associated to the surface defect density of the specimens also in the frame of Ti6Al4V L-PBF specimens, as previously done also for aluminum alloys [67,68]. The trend reported in Fig. 11b is in line with this hypothesis, since higher $1-\alpha$ values are reported for lower inclined specimens (15° and 0°), which reports higher defect sensitivity, i.e., high surface texture [19], if compared to vertical specimens, conversely reporting a higher printing accuracy, as also previously discussed.

To further check the sensitivity to the mean stress effect, the increment in percentage between each stress ratio for the same building orientation has been also listed in Table 5. This percentage (calculated for different cycles) is obtained by fixing as reference the lowest fatigue value, therefore the tension–tension fatigue condition. From these data, it is possible to further understand the impact of the mean stress effect on the different oriented batches. It is indeed evincible, from Table 5, how beneficial the introduction of a compressive state in the fatigue loading regime of inclined and horizontal struts is. Particularly, when $\sigma_m < 0$, the compressive regime is predominant (R = −84 and R = 10) and increases of twice or even three times over the R = 0.1 fatigue life are registered. Among these three batches, 15° and 0° appear to be more sensitive to the mean stress effect than the 45° oriented struts. At R = −4, more pronounced increases at 10^7 cycles are indeed appreciated, respectively of 220 %, for 15° struts, 267 %, for 0° struts, with respect to the 133 % of 45° specimens.

Table 5
Percentage data of the increment of the fatigue strength from R = 0.1 to R = 10. The percentage increments are calculated considering the four predefined number of cycles, namely at 10^4, 10^5, 10^6 and 10^7 cycles. For the compression-compression fatigue, the stress amplitude data reported in the Haigh Diagram are considered.

Building orientation	R	Increment at $\sigma_{a,50\%}$ @10^4 (%)	Increment at $\sigma_{a,50\%}$ @10^5 (%)	Increment at $\sigma_{a,50\%}$ @10^6 (%)	Increment at $\sigma_{a,50\%}$ @10^7 (%)
90°	0.1	–	–	–	–
	−1	−14	27	32	29
	−4	13	37	39	38
	10	–	151	199	204
45°	0.1	–	–	–	–
	−1	−14	37	71	87
	−4	123	128	131	133
	10	–	–	–	289
15°	0.1	–	–	–	–
	−1	31	48	67	89
	−4	174	158	181	220
	10	–	–	–	273
0°	0.1	–	–	–	–
	−1	40	38	51	73
	−4	370	170	200	267
	10	–	–	–	351

Conversely, vertical struts exhibit a lower influence on the mean stress effect, since increments always below 50 % are detectable, respectively for R = −1 or R = −4. The milder effect of mean stress on vertical specimens can be ascribable to the combined role of porosity, degree of defectiveness, and residual stresses discussed in the previous sections.

Haigh Diagrams (σ_a vs σ_m) in Fig. 12a. These data are further normalized with respect to the associated experimental yield strength (σ_y) in Fig. 12b. It is essential to note that the reported data refers to L-PBF specimens in the as-built condition, which have undergone similar heat treatments of stress relieving and annealing to achieve an α + β acicular microstructure. The only exception is for the work of *Bendetti et al.* [39], where specimens only underwent stress relieving treatment, retaining their α' state (labeled with an asterisk in Fig. 12). Each data point included in the graphs also show the nominal diameter of the coupon specimen. The scarcity of fatigue data of miniaturized L-PBF Ti6Al4V specimens available in literature cannot allow to have a direct comparison at the sub-millimeter scale. For instance, specimens indicated as miniaturized in the work of *Cutolo et al.* [41] shows a nominal diameter of 2.5 mm, making them 3.4 times larger than those in this study. The size of the specimen seems to significantly influence the fatigue properties of L-PBF components in their as-built state, probably due to the different surface-to-volume ratio and its effect on surface defect sensitivity. Unmolten or partially melted particles on the strut surface have a more pronounced negative impact on sub-millimetric scale specimens, affecting both the presence of"killer" defects for fatigue failure and the "real" load-bearing area, more so than in the millimetric scale specimens. Interestingly, the size effect is apparent across all the investigated stress ratios, covering tension-tension to predominantly compressive fatigue regimes. However, further investigations are warranted especially in the compressive regime, due to the limited data availability. This trend is corroborated by the normalized Haigh Diagram (Fig. 12b), suggesting that it may be a characteristic feature of the fatigue behavior of AM as-built components. Nevertheless, it is important to recognize that the "size effect" is not the sole or primary mechanisms driving this differential fatigue behavior. Processing parameters, such as powder size, layer thickness, scanning speed, significantly contribute to the variability in the fatigue performances of AM struts, due to their relevant influence on their morphological outcome.

4. Conclusions

In this work, the monotonic and fatigue behavior of L-PBF Ti-6Al-4V thin struts with miniaturized dimensions were investigated according to four different building directions. A particular focus was addressed on the fatigue strength of these specimens under different loading conditions, varying from tension-tension to compression-compression regimes. Haigh diagrams to investigate the mean stress effect for the different printing inclinations were evaluated. Moreover, the buckling instabilities and the potential different fatigue failure mechanisms were discussed on the fracture surfaces of the investigated specimens. The

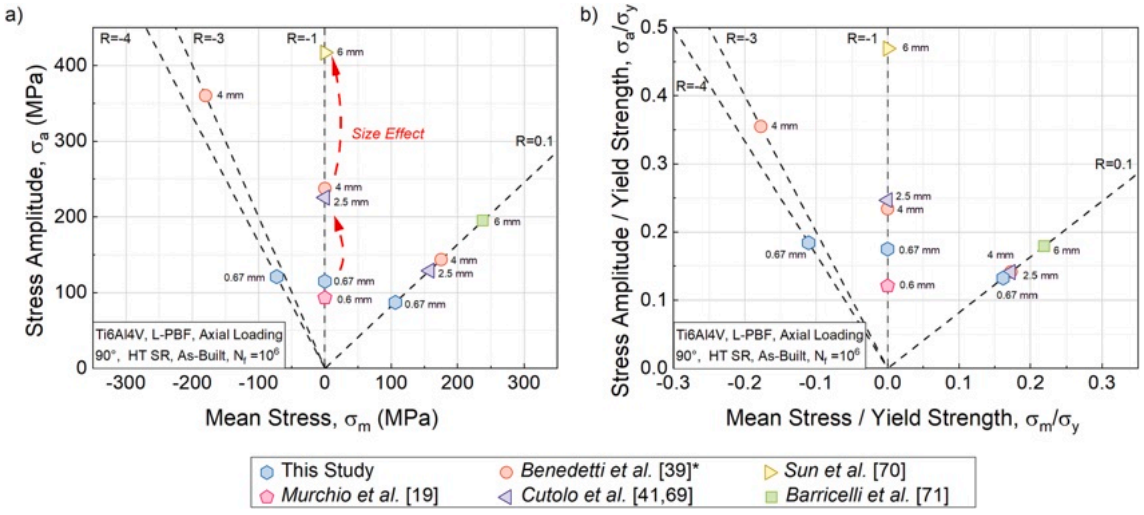

Fig. 12. High Diagrams (a) and normalized Haigh diagrams over experimental yield strength (b) for Ti6Al4V L-PBF 90° strut specimens at 10^6 cycles comparing the data from this study (blue hexagons) with literature data from [19] (pink hexagons, 0.6 mm nominal diameter), [39] (orange circles, 4 mm nominal diameter), [41,69] (purple left-oriented triangle, nominal diameter 2.5 mm), [70] (yellow right-oriented triangles, 6 mm nominal diameter) and [71] (green square, 6 mm nominal diameter). Data reported in this graph refers to L-PBF specimens which have undergone comparable stress relieving and annealing heat treatment. * Indicates that only stress relieving heat treatment has been performed, retaining the α' structure. Each datum reports the nominal strut diameter in the graph and is placed along the stress ratio under which it was fatigue tested. Reported stress ratios are R = -1, R = 0.1, R = -3 and R = -4.

results of this work and the associated conclusions can be summarized as follow:

- The fatigue strength of thin struts is strongly influenced by the stress ratio with an increase in the fatigue life, the higher the compressive load is. This can be imputed to the closing crack stresses which partially hinder the crack propagation from the surface, main source of defects for miniaturized as-built struts.
- The building orientation affects the fatigue life of the specimens according to different trends as function of the stress ratio. In tension–tension, it registered a decreasing trend moving from the 90° to the 0° thin struts, while for R = −4, the trend is reversed. In the compression-compression regime, the building orientation trend is again flipped, and it is mainly ruled by buckling instabilities. Thin strut specimens are indeed more prone to fail due to buckling or to report a run out at 10^7 cycles, rather than failing due to fatigue.
- Fracture surface analysis showed that surface defects are the main driving mechanism for fatigue failure in tension. Conversely, when the compressive load becomes predominant in the fatigue cycle, i.e., at R = −4, vertical specimens report a stronger influence of the subsurface and internal defects as principal crack nucleation site. Indeed, these specimens exhibited the highest defect density over the CT-scanned volume, as well as the largest potential "killer" defects. This might explain the inversion of trend as function of the building orientation angle in a predominantly compressive fatigue regime.
- The mean stress effect has been investigated by employing the Haigh diagram, revealing a good agreement of the experimental data with the SWT method. This outcome shows the importance of maximum stress, into the fatigue life evaluation and prediction of thin strut specimens.
- The effect of buckling instabilities on the fatigue behavior of thin struts is also accounted for each investigated orientation. An additional unsafe designing area, where buckling instabilities can occur, is included in the Haigh diagram, considering the Johnson's critical buckling stress as maximum allowable stress.
- The Walker method has been also considered to investigate the different mean stress sensitivity. Interestingly, an inverse trend of the Walker's coefficient, $1-\alpha$, as function of the building orientation is shown, suggesting a lower dependency of vertical specimens to the mean stress. This might be associated to the better printing accuracy and lower surface defects of this batch of specimens.
- These outcomes have the potential to contribute to the development of effective tools and guidelines for informed design and manufacturing of as-built lattice-based devices. For instance, they can play a fundamental role on the development of optimization strategies focused on identifying the optimal building orientation for enhancing the fatigue resistance of lattice-based components. An example of such a study is presented in the work by *De Biasi et al.* [72]. As a future scope, the incorporation of the mean stress effect as a function of the building orientation could be crucial for its further refinement.

CRediT authorship contribution statement

Simone Murchio: . **Anton Du Plessis:** Investigation, Software, Writing – original draft. **Valerio Luchin:** . **Devid Maniglio:** Funding acquisition, Resources, Supervision. **Matteo Benedetti:** .

Declaration of competing interest

The authors declare that they have no known competing financial interests or personal relationships that could have appeared to influence the work reported in this paper.

Data availability

Data will be made available on request.

Acknowledgments

The authors would like to thank Dr. Gianluca Zappini from Lincotek Medical (Trento, Italy) for his contribution to the design of specimens and for their fabrication, Mr. Luca De Nart and Mr. Andrea Rigatti for the help with the fatigue testing of the specimens. This project has received funding from the Italian Ministry for Education, University, and Research (MIUR) within the program "Departments of Excellence" 2018–2022 (DII-UNITN) and through the REGENERA project.

Appendix A. Supplementary data

Supplementary data to this article can be found online at https://doi.org/10.1016/j.ijfatigue.2023.108102.

References

[1] du Plessis A, Razavi SMJ, Benedetti M, Murchio S, Leary M, Watson M, et al. Properties and applications of additively manufactured metallic cellular materials: A review. Prog Mater Sci 2022;125:100918. https://doi.org/10.1016/j.pmatsci.2021.100918.
[2] Al-Ketan O, Rowshan R, Abu Al-Rub RK. Topology-mechanical property relationship of 3D printed strut, skeletal, and sheet based periodic metallic cellular materials. Addit Manuf 2018;19:167–83. https://doi.org/10.1016/j.addma.2017.12.006.
[3] Loh GH, Pei E, Harrison D, Monzón MD. An overview of functionally graded additive manufacturing. Addit Manuf 2018;23:34–44. https://doi.org/10.1016/j.addma.2018.06.023.
[4] Murr LE. Additive manufacturing of biomedical devices: an overview. Mater Technol 2018;33:57–70.
[5] Moussa A, Tanzer M, Pasini D. Cervical fusion cage computationally optimized with porous architected Titanium for minimized subsidence. J Mech Behav Biomed Mater 2018;85:134–51. https://doi.org/10.1016/j.jmbbm.2018.05.040.
[6] Barba D, Alabort E, Reed RC. Synthetic bone: Design by additive manufacturing. Acta Biomater 2019;97:637–56. https://doi.org/10.1016/j.actbio.2019.07.049.
[7] Willemsen K, Nizak R, Noordmans HJ, Castelein RM, Weinans H, Kruyt MC. Challenges in the design and regulatory approval of 3D-printed surgical implants: a two-case series. Lancet Digit Heal 2019;1:e163–71.
[8] Noronha J, Rogers J, Leary M, Kyriakou E, Inverarity S, Das R, et al. Ti-6Al-4V hollow-strut lattices by laser powder bed fusion. Addit Manuf 2023:103637.
[9] Ricles LM, Coburn JC, Di Prima M, Oh SS. Regulating 3D-printed medical products. Sci Transl Med 2018;10:eaan6521.
[10] Di Prima M, Coburn J, Hwang D, Kelly J, Khairuzzaman A, Ricles L. Additively manufactured medical products–the FDA perspective, 3D Print. Med 2016;2:1–6.
[11] Khorasani AM, Gibson I, Ghasemi A, Ghaderi A. Modelling of laser powder bed fusion process and analysing the effective parameters on surface characteristics of Ti-6Al-4V. Int J Mech Sci 2020;168:105299.
[12] Soro N, Saintier N, Merzeau J, Veidt M, Dargusch MS. Quasi-static and fatigue properties of graded Ti–6Al–4V lattices produced by Laser Powder Bed Fusion (LPBF). Addit Manuf 2021;37:101653.
[13] Chen W, Yang J, Kong H, Helou M, Zhang D, Zhao J, et al. Fatigue behaviour and biocompatibility of additively manufactured bioactive tantalum graded lattice structures for load-bearing orthopaedic applications. Mater Sci Eng C 2021;130:112461.
[14] Lietaert K, Cutolo A, Boey D, Van Hooreweder B. Fatigue life of additively manufactured Ti6Al4V scaffolds under tension-tension, tension-compression and compression-compression fatigue load. Sci Rep 2018;8:1–9. https://doi.org/10.1038/s41598-018-23414-2.
[15] Dallago M, Winiarski B, Zanini F, Carmignato S, Benedetti M. On the effect of geometrical imperfections and defects on the fatigue strength of cellular lattice structures additively manufactured via Selective Laser Melting. Int J Fatigue 2019;124:348–60. https://doi.org/10.1016/j.ijfatigue.2019.03.019.
[16] Zhang Z, Xu Z. Fatigue database of additively manufactured alloys. Sci Data 2023;10:1–15. https://doi.org/10.1038/s41597-023-02150-x.
[17] Zeng Y, Li M, Zhou Y, Li N. Development of a new method for estimating the fatigue life of notched specimens based on stress field intensity. Theor Appl Fract Mech 2019;104:102339. https://doi.org/10.1016/j.tafmec.2019.102339.
[18] Lazzarin P, Livieri P, Berto F, Zappalorto M. Local strain energy density and fatigue strength of welded joints under uniaxial and multiaxial loading. Eng Fract Mech 2008;75:1875–89. https://doi.org/10.1016/j.engfracmech.2006.10.019.
[19] Murchio S, Dallago M, Zanini F, Carmignato S, Zappini G, Berto F, et al. Additively manufactured Ti–6Al–4V thin struts via laser powder bed fusion: Effect of building orientation on geometrical accuracy and mechanical properties. J Mech Behav Biomed Mater 2021;119. https://doi.org/10.1016/j.jmbbm.2021.104495.
[20] Murchio S, Dallago M, Rigatti A, Luchin V, Berto F, Maniglio D, et al. On the effect of the node and building orientation on the fatigue behavior of L-PBF Ti6Al4V

lattice structure sub-unital elements. Mater Des Process Commun 2021;3:1–9. https://doi.org/10.1002/mdp2.258.
[21] Persenot T, Burr A, Martin G, Buffiere JY, Dendievel R, Maire E. Effect of build orientation on the fatigue properties of as-built Electron Beam Melted Ti-6Al-4V alloy. Int J Fatigue 2019;118:65–76. https://doi.org/10.1016/j.ijfatigue.2018.08.006.
[22] Persenot T, Burr A, Dendievel R, Buffière JY, Maire E, Lachambre J, et al. Fatigue performances of chemically etched thin struts built by selective electron beam melting: Experiments and predictions. Materialia 2020;9:100589. https://doi.org/10.1016/j.mtla.2020.100589.
[23] Wan HY, Yang WK, Wang LY, Zhou ZJ, Li CP, Chen GF, et al. Toward qualification of additively manufactured metal parts: Tensile and fatigue properties of selective laser melted Inconel 718 evaluated using miniature specimens. J Mater Sci Technol 2022;97:239–53. https://doi.org/10.1016/j.jmst.2021.04.049.
[24] Hossain U, Ghouse S, Nai K, Jeffers JRT. Mechanical and morphological properties of additively manufactured SS316L and Ti6Al4V micro-struts as a function of build angle. Addit Manuf 2021;46:102050.
[25] Dzugan J, Seifi M, Prochazka R, Rund M, Podany P, Konopik P, et al. Effects of thickness and orientation on the small scale fracture behaviour of additively manufactured Ti-6Al-4V. Mater Charact 2018;143:94–109. https://doi.org/10.1016/j.matchar.2018.04.003.
[26] Zhang L, Harrison W, Yar MA, Brown SGR, Lavery NP. The development of miniature tensile specimens with non-standard aspect and slimness ratios for rapid alloy prototyping processes. J Mater Res Technol 2021;15:1830–43. https://doi.org/10.1016/j.jmrt.2021.09.029.
[27] Du Plessis A, Beretta S. Killer notches: The effect of as-built surface roughness on fatigue failure in AlSi10Mg produced by laser powder bed fusion. Addit Manuf 2020;35:101424.
[28] Maleki E, Bagherifard S, Bandini M, Guagliano M. Surface post-treatments for metal additive manufacturing: Progress, challenges, and opportunities. Addit Manuf 2021;37:101619. https://doi.org/10.1016/j.addma.2020.101619.
[29] Whip B, Sheridan L, Gockel J. The effect of primary processing parameters on surface roughness in laser powder bed additive manufacturing. Int J Adv Manuf Technol 2019;103:4411–22.
[30] Yin K, Cao B, Todt J, Gutmann F, Tunçay HF, Roth A, et al. Manufacturing size effect on the structural and mechanical properties of additively manufactured Ti-6Al-4V microbeams. J Mater Sci Technol 2023;149:18–30. https://doi.org/10.1016/j.jmst.2022.12.006.
[31] Mullen L, Stamp RC, Fox P, Jones E, Ngo C, Sutcliffe CJ. Selective laser melting: A unit cell approach for the manufacture of porous, titanium, bone in-growth constructs, suitable for orthopedic applications. II Randomized structures. J Biomed Mater Res - Part B Appl Biomater 2009;92:178–88. https://doi.org/10.1002/jbm.b.31504.
[32] Pyka G, Kerckhofs G, Papantoniou I, Speirs M, Schrooten J, Wevers M. Surface Roughness and Morphology Customization of Additive Manufactured Open Porous Ti6Al4V Structures. Materials (Basel) 2013;6:4737–57. https://doi.org/10.3390/ma6104737.
[33] Bagheri ZS, Melancon D, Liu L, Johnston RB, Pasini D. Compensation strategy to reduce geometry and mechanics mismatches in porous biomaterials built with Selective Laser Melting. J Mech Behav Biomed Mater 2017;70:17–27. https://doi.org/10.1016/j.jmbbm.2016.04.041.
[34] Yan C, Hao L, Hussein A, Young P, Raymont D. Advanced lightweight 316L stainless steel cellular lattice structures fabricated via selective laser melting. Mater Des 2014;55:533–41. https://doi.org/10.1016/j.matdes.2013.10.027.
[35] Wu Z, Wu S, Bao J, Qian W, Karabal S, Sun W, et al. The effect of defect population on the anisotropic fatigue resistance of AlSi10Mg alloy fabricated by laser powder bed fusion. Int J Fatigue 2021;151:106317. https://doi.org/10.1016/j.ijfatigue.2021.106317.
[36] Carrion PE, Sausto F, Beretta S, Shamsaei N. Multiaxial fatigue behavior and modelling of additive manufactured Ti-6Al-4V parts: The effects of layer orientation and surface texture. Int J Fatigue 2023;176:107860. https://doi.org/10.1016/j.ijfatigue.2023.107860.
[37] de Krijger J, Rans C, Van Hooreweder B, Lietaert K, Pouran B, Zadpoor AA. Effects of applied stress ratio on the fatigue behavior of additively manufactured porous biomaterials under compressive loading. J Mech Behav Biomed Mater 2017;70:7–16.
[38] Yavari SA, Ahmadi SM, Wauthle R, Pouran B, Schrooten J, Weinans H, et al. Relationship between unit cell type and porosity and the fatigue behavior of selective laser melted meta-biomaterials. J Mech Behav Biomed Mater 2015;43:91–100.
[39] Benedetti M, Fontanari V, Bandini M, Zanini F, Carmignato S. Low-and high-cycle fatigue resistance of Ti-6Al-4V ELI additively manufactured via selective laser melting: Mean stress and defect sensitivity. Int J Fatigue 2018;107:96–109.
[40] Derrick C, Fatemi A. Correlations of fatigue strength of additively manufactured metals with hardness and defect size. Int J Fatigue 2022;162:106920. https://doi.org/10.1016/j.ijfatigue.2022.106920.
[41] Cutolo A, Elangeswaran C, Van Hooreweder B. On the Effect of the Stress Ratio on Fatigue Properties of Ti-6Al-4V Produced by Laser Powder Bed Fusion. Mater Des Process Commun 2022;2022:1–7. https://doi.org/10.1155/2022/3530603.
[42] Pilkey WD, Pilkey DF. Peterson's Stress Concentration Factors. John Wiley & Sons; 2008.
[43] Dallago M, Raghavendra S, Luchin V, Zappini G, Pasini D, Benedetti M. Geometric assessment of lattice materials built via Selective Laser Melting. Mater Today Proc 2019;7:353–61. https://doi.org/10.1016/j.matpr.2018.11.096.
[44] Nagalingam AP, Vohra MS, Kapur P, Yeo SH. Effect of cut-off, evaluation length, and measurement area in profile and areal surface texture characterization of as-built metal additive manufactured components. Appl Sci 2021;11. https://doi.org/10.3390/app11115089.
[45] Van Hooreweder B, Lietaert K, Neirinck B, Lippiatt N, Wevers M. CoCr F75 scaffolds produced by additive manufacturing: Influence of chemical etching on powder removal and mechanical performance. J Mech Behav Biomed Mater 2017;70:60–7. https://doi.org/10.1016/j.jmbbm.2017.03.017.
[46] McGee OM, Geraghty S, Hughes C, Jamshidi P, Kenny DP, Attallah MM, et al. An investigation into patient-specific 3D printed titanium stents and the use of etching to overcome Selective Laser Melting design constraints. J Mech Behav Biomed Mater 2022;134:105388. https://doi.org/10.1016/j.jmbbm.2022.105388.
[47] Alghamdi A, Downing D, Tino R, Almalki A, Maconachie T, Lozanovski B, et al. Buckling phenomena in AM lattice strut elements: A design tool applied to Ti-6Al-4V LB-PBF. Mater Des 2021;208:109892. https://doi.org/10.1016/j.matdes.2021.109892.
[48] Hänel B. Analytical strength assessment–FKM guideline. 5th ed. 2003.
[49] Murakami Y, Beretta S. Small defects and inhomogeneities in fatigue strength: experiments, models and statistical implications. Extremes 1999;2:123–47.
[50] Coles S, Bawa J, Trenner L, Dorazio P. An introduction to statistical modeling of extreme values. Springer; 2001.
[51] Romano S, Brandão A, Gumpinger J, Gschweitl M, Beretta S. Qualification of AM parts: Extreme value statistics applied to tomographic measurements. Mater Des 2017;131:32–48.
[52] Beretta S. More than 25 years of extreme value statistics for defects: Fundamentals, historical developments, recent applications. Int J Fatigue 2021;151:106407. https://doi.org/10.1016/j.ijfatigue.2021.106407.
[53] Romano S, Abel A, Gumpinger J, Brandão AD, Beretta S. Quality control of AlSi10Mg produced by SLM: Metallography versus CT scans for critical defect size assessment. Addit Manuf 2019;28:394–405. https://doi.org/10.1016/j.addma.2019.05.017.
[54] Phutela C, Aboulkhair NT, Tuck CJ, Ashcroft I. The effects of feature sizes in selectively laser melted Ti-6Al-4V parts on the validity of optimised process parameters. Materials (Basel) 2020;13:117. https://doi.org/10.3390/ma13010117.
[55] Hu YN, Wu SC, Wu ZK, Zhong XL, Ahmed S, Karabal S, et al. A new approach to correlate the defect population with the fatigue life of selective laser melted Ti-6Al-4V alloy. Int J Fatigue 2020;136. https://doi.org/10.1016/j.ijfatigue.2020.105584.
[56] Agius D, Kourousis KI, Wallbrink C, Song T. Cyclic plasticity and microstructure of as-built SLM Ti-6Al-4V: The effect of build orientation. Mater Sci Eng A 2017;701:85–100. https://doi.org/10.1016/j.msea.2017.06.069.
[57] Kan WH, Chiu LNS, Lim CVS, Zhu Y, Tian Y, Jiang D, et al. A critical review on the effects of process-induced porosity on the mechanical properties of alloys fabricated by laser powder bed fusion. J Mater Sci 2022;57:9818–65.
[58] Benedetti M, Du Plessis A, Ritchie RO, Dallago M, Razavi SMJ, Berto F. Architected cellular materials: A review on their mechanical properties towards fatigue-tolerant design and fabrication. Mater Sci Eng R Reports 2021;144:100606.
[59] Kelly CN, Kahra C, Maier HJ, Gall K. Processing, structure, and properties of additively manufactured titanium scaffolds with gyroid-sheet architecture. Addit Manuf 2021;41:101916. https://doi.org/10.1016/j.addma.2021.101916.
[60] Ye J, Poudel A, J. (Peter) Liu, A. Vinel, D. Silva, S. Shao, N. Shamsaei,. Machine learning augmented X-ray computed tomography features for volumetric defect classification in laser beam powder bed fusion. Int J Adv Manuf Technol 2023;126:3093–107. https://doi.org/10.1007/s00170-023-11281-9.
[61] Peng X, Wu S, Qian W, Bao J, Hu Y, Zhan Z, et al. The potency of defects on fatigue of additively manufactured metals. Int J Mech Sci 2022;221:107185. https://doi.org/10.1016/j.ijmecsci.2022.107185.
[62] Barba D, Alabort C, Tang YT, Viscasillas MJ, Reed RC, Alabort E. On the size and orientation effect in additive manufactured Ti-6Al-4V. Mater Des 2020;186:108235. https://doi.org/10.1016/j.matdes.2019.108235.
[63] O'Keeffe C, Taylor D, Lally C, Kelly DJ. Morphological induced improvements in the bulk mechanical properties of chemically etched additively manufactured Ti-6Al-4V micro-struts. Addit Manuf 2023;75:103748. https://doi.org/10.1016/j.addma.2023.103748.
[64] Dong Z, Zhang X, Shi W, Zhou H, Lei H, Liang J. Study of size effect on microstructure and mechanical properties of AlSi10Mg samples made by selective laser melting. Materials (Basel) 2018;11:2463.
[65] Sombatmai A, Uthaisangsuk V, Wongwises S, Promoppatum P. Multiscale investigation of the influence of geometrical imperfections, porosity, and size-dependent features on mechanical behavior of additively manufactured Ti-6Al-4V lattice struts. Mater Des 2021;209:109985.
[66] Dowling NE, Calhoun CA, Arcari A. Mean stress effects in stress-life fatigue and the Walker equation. Fatigue Fract Eng Mater Struct 2009;32:163–79.
[67] Houria MI, Nadot Y, Fathallah R, Roy M, Maijer DM. Influence of casting defect and SDAS on the multiaxial fatigue behaviour of A356–T6 alloy including mean stress effect. Int J Fatigue 2015;80:90–102.
[68] Gall K, Horstemeyer MF, Degner BW, McDowell DL, Fan J. On the driving force for fatigue crack formation from inclusions and voids in a cast A356 aluminum alloy. Int J Fract 2001;108:207–33.
[69] Cutolo A, Elangeswaran C, Muralidharan GK, Van Hooreweder B. On the role of building orientation and surface post-processes on the fatigue life of Ti-6Al-4V coupons manufactured by laser powder bed fusion. Mater Sci Eng A 2022;840:142747. https://doi.org/10.1016/j.msea.2022.142747.

[70] Sun W, Ma Y, Huang W, Zhang W, Qian X. Effects of build direction on tensile and fatigue performance of selective laser melting Ti6Al4V titanium alloy. Int J Fatigue 2020;130. https://doi.org/10.1016/j.ijfatigue.2019.105260.
[71] Barricelli L, Patriarca L, du Plessis A, Beretta S. Orientation-dependent fatigue assessment of Ti6Al4V manufactured by L-PBF: Size of surface features and shielding effect. Int J Fatigue 2023;168:107401. https://doi.org/10.1016/j.ijfatigue.2022.107401.
[72] De Biasi R, Murchio S, Sbettega E, Carmignato S, Luchin V, Benedetti M. Efficient optimization framework for L-PBF fatigue enhanced Ti6Al4V lattice component. Mater Des 2023;230:111975. https://doi.org/10.1016/j.matdes.2023.111975.